Comput Mech (2009) 45:23–44
DOI 10.1007/s00466-009-0415-2

ORIGINAL PAPER

An edge-based smoothed finite element method for visco-elastoplastic analyses of 2D solids using triangular mesh

T. Nguyen-Thoi · G. R. Liu · H. C. Vu-Do · H. Nguyen-Xuan

Received: 16 March 2009 / Accepted: 19 August 2009 / Published online: 16 September 2009

Abstract An edge-based smoothed finite element method (ES-FEM) using triangular elements was recently proposed to improve the accuracy and convergence rate of the existing standard finite element method (FEM) for the elastic solid mechanics problems. In this paper, the ES-FEM is extended to more complicated visco-elastoplastic analyses using the von-Mises yield function and the Prandtl–Reuss flow rule. The material behavior includes perfect visco-elastoplasticity and visco-elastoplasticity with isotropic and linear kinematic hardening. The formulation shows that the bandwidth of stiffness matrix of the ES-FEM is larger than that of the FEM, and hence the computational cost of the ES-FEM in numerical examples is larger than that of the FEM for the same mesh. However, when the efficiency of computation (computation time for the same accuracy) in terms of a posteriori error estimation is considered, the ES-FEM is more efficient than the FEM.

Keywords Numerical methods · Edge-based smoothed finite element method (ES-FEM) · Finite element method (FEM) · Strain smoothing technique · Visco-elastoplastic analysis

T. Nguyen-Thoi (✉) · G. R. Liu · H. C. Vu-Do
Department of Mechanical Engineering, Center for Advanced Computations in Engineering Science (ACES), National University of Singapore, 9 Engineering Drive 1, Singapore 117576, Singapore
e-mail: ngttrung@hcmuns.edu.vn; thoitrung76@yahoo.com

G. R. Liu · H. Nguyen-Xuan
Singapore-MIT Alliance (SMA), E4-04-10, 4 Engineering Drive 3, Singapore 117576, Singapore

T. Nguyen-Thoi · H. C. Vu-Do · H. Nguyen-Xuan
Faculty of Mathematics and Computer Science, University of Science, Vietnam National University-HCM, 227 Nguyen Van Cu, District 5, Ho Chi Minh City, Vietnam

1 Introduction

The strain smoothing technique [4] has been proposed to stabilize the solutions in the context of the meshfree method and then applied in the natural element method [31]. Liu et al. has generalized the gradient (strain) smoothing technique [9] and applied it in the meshfree context to formulate the node-based smoothed point interpolation method (NS-PIM or LC-PIM) [17,18] and the linearly conforming radial point interpolation method (NS-RPIM or LC-RPIM) [11]. Applying the same idea to FEM, a cell-based smoothed finite element method (SFEM or CS-FEM) [10,12] and a node-based smoothed finite element method (NS-FEM) [15] have also been formulated.

In the CS-FEM, the strain smoothing domains and the integration are performed over the quadrilateral elements, and these smoothing domains can be divided into one or many smoothing cells (SC) on each element, as shown in Fig. 1. When the number of SC of the elements equals 1, the CS-FEM solution has the same properties with those of FEM using reduced integration. When SC approaches infinity, the CS-FEM solution approaches to the solution of the standard displacement compatible FEM model [12]. In practical calculation, using four SCs for each quadrilateral element in the CS-FEM is easy to implement, work well in general and hence advised for all problems. The numerical solution of CS-FEM (SC = 4) is always stable, accurate, much better than FEM, and often very close to the exact solutions. The CS-FEM has been developed for general n-sided polygonal elements (nSFEM or nCS-FEM) [7], dynamic analyses [6], incompressible materials using selective integration [20,25], plate and shell analyses [5,19,24,28,29], and further extended for the extended finite element method (XFEM) to solve fracture mechanics problems in 2D continuum and plates [1].

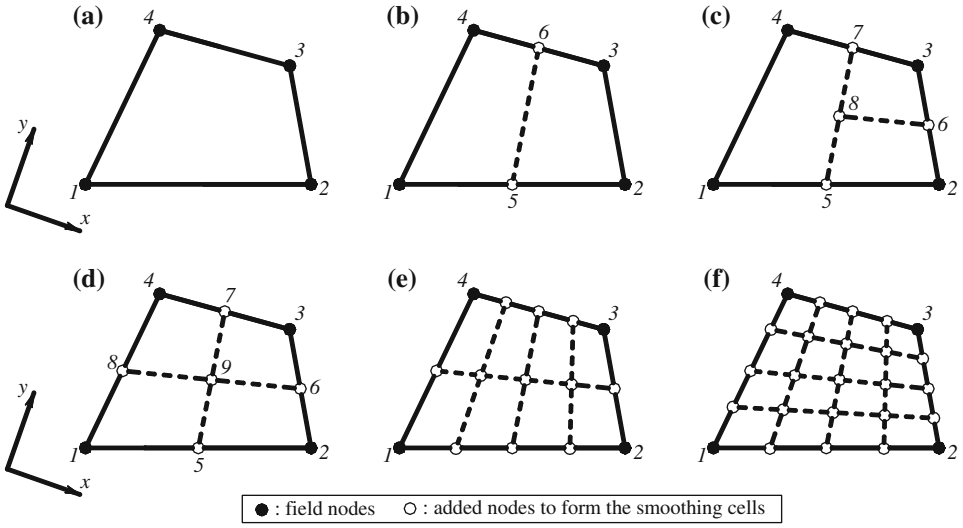

Fig. 1 Division of quadrilateral element into the smoothing cells (SCs) in the CS-FEM by connecting the mid-edge-points of opposite edges of SCs. **a** 1 SC; **b** 2 SCs; **c** 3 SCs; **d** 4 SCs; **e** 8 SCs; **f** 16 SCs

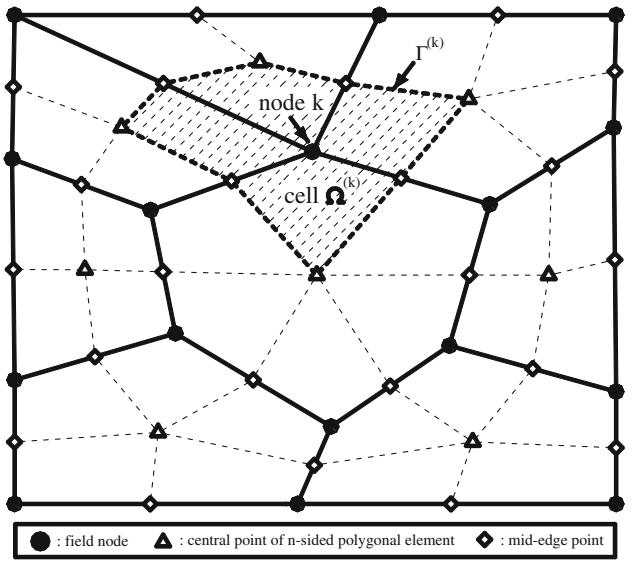

Fig. 2 *n*-Sided polygonal elements and the smoothing cell (*shaded area*) associated with nodes in the NS-FEM

In the NS-FEM, the strain smoothing domains and the integration of the weak form are performed over the cells associated with nodes, and methods can be applied easily to triangular, 4-node quadrilateral, *n*-sided polygonal elements for 2D problems and tetrahedral elements for 3D problems. For *n*-sided polygonal elements, the cell $\Omega^{(k)}$ associated with the node k is created by connecting sequentially the mid-edge-point to the central points of the surrounding *n*-sided polygonal elements of the node k as shown in Fig. 2. When only linear triangular or tetrahedral elements are used, the NS-FEM produces the same results as the method proposed by Dohrmann et al. [8] or to the LC-PIM [17] using linear interpolation. The upper bound property shown in the NS-PIM [16] was also found in the NS-FEM [15]. Then, by combing the NS-FEM, FEM and a scale factor $\alpha \in [0, 1]$, a so-called the alpha Finite Element Method (αFEM) [13] using triangular and tetrahedral elements is proposed to give a nearly exact solution in strain energy. The NS-FEM has been developed for adaptive analysis [22].

Recently, an edge-based smoothed finite element method (ES-FEM) [14] was also been formulated for static, free and forced vibration analyses in 2D problems. The ES-FEM uses triangular elements that can be generated automatically for complicated domains. In the ES-FEM, the system stiffness matrix is computed using strains smoothed over the smoothing domains associated with the edges of the triangles. For triangular elements, the smoothing domain $\Omega^{(k)}$ associated with the edge k is created by connecting two endpoints of the edge to the centroids of the adjacent elements as shown in Fig. 3. The numerical results demonstrated that the ES-FEM possesses the following excellent properties: (1) the numerical results are often found super-convergent and much more accurate than those of FEM using quadrilateral elements with the same sets of nodes; (2) there are no spurious non-zeros energy modes found and hence the method is also stable and works well for vibration analysis; (3) the implementation of the method is straightforward and no penalty parameter is used, and the computational efficiency is better than FEM using the same sets of nodes; (4) a novel domain-based selective scheme is proposed leading to a combined ES/NS-FEM model that is immune from volumetric locking and hence works very well for nearly incompressible materials. The ES-FEM has been developed for 2D piezoelectric [26], plate [27] and primal-dual shakedown analyses [30]. The idea of the ES-FEM is also quite straightforward to extend for the 3D problems using tetrahedral elements to give a so-called the face-based smoothed finite element method (FS-FEM) [21,23].

In this paper, we aim to extend the ES-FEM to even more complicated visco-elastoplastic analyses in the solid

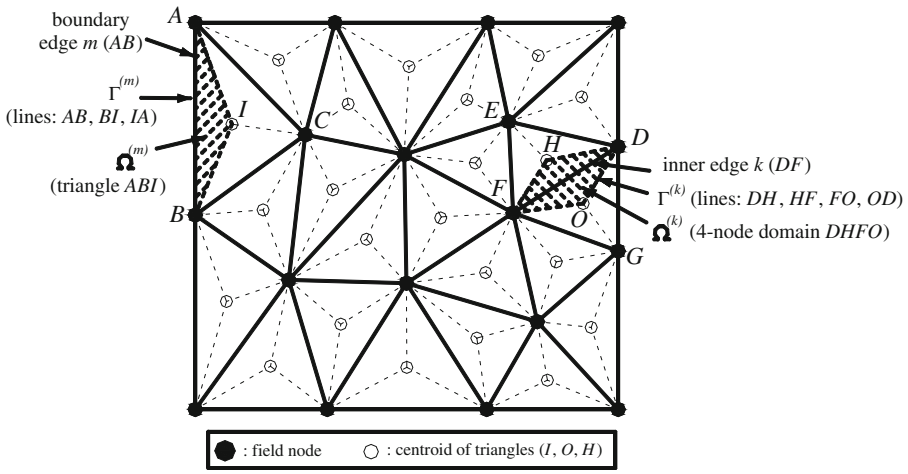

Fig. 3 Triangular elements and the smoothing domains (*shaded areas*) associated with edges in the ES-FEM

mechanics. In this work, we combine the ES-FEM with the work of Carstensen and Klose [2] using the standard FEM in the setting of von-Mises conditions and the Prandtl–Reuss flow rule. The material behavior includes perfect visco-elastoplasticity and visco-elastoplasticity with isotropic and linear kinematic hardening in a dual model with both displacements and the stresses as the main variables. The numerical procedure, however, eliminates the stress variables and the problem becomes only displacement-dependent and is much easy to deal with. The formulation shows that the bandwidth of stiffness matrix of the ES-FEM is larger than that of FEM, and hence the computational cost of the ES-FEM in numerical examples is larger than that of the FEM. However, when the efficiency of computation (computation time for the same accuracy) in terms of a posteriori error estimation is considered, the ES-FEM is more efficient than the FEM.

2 Dual model of visco-elastoplastic problem using the ES-FEM

2.1 Strong form and weak form [2]

The strong form of the visco-elastoplastic problem which deforms in the interval $t \in [0, T]$ can be described by equilibrium equation in the domain Ω bounded by Γ

$$\mathrm{div}\boldsymbol{\sigma} + \mathbf{b} = \mathbf{0} \quad \text{in } \Omega \tag{1}$$

where $\mathbf{b} \in (\mathbb{L}_2(\Omega))^2$ is the body forces, $\boldsymbol{\sigma} \in (\mathbb{L}_2(\Omega))^3$ is the stress field. The essential and static boundary conditions, respectively, on the Dirichlet boundary Γ_D and the Neumann boundary Γ_N are

$$\mathbf{u} = \mathbf{w}_0 \quad \text{on } \Gamma_D \quad \text{and } \boldsymbol{\sigma}\mathbf{n} = \bar{\mathbf{t}} \quad \text{on } \Gamma_N \tag{2}$$

in which $\mathbf{u} \in (\mathbb{H}^1(\Omega))^2$ is the displacement field; $\mathbf{w}_0 \in (\mathbb{H}^1(\Omega))^2$ is prescribed surface displacement; $\bar{\mathbf{t}} \in (\mathbb{L}_2(\Gamma_N))^2$ is prescribed surface force and $\mathbf{n}$ is the unit outward normal matrix.

In the context of small strain, the total strain $\boldsymbol{\varepsilon}(\mathbf{u}) = \nabla_S\mathbf{u}$, where $\nabla_S\mathbf{u}$ denotes the symmetric part of displacement gradient, is separated into two contributions

$$\boldsymbol{\varepsilon}(\mathbf{u}) = \mathbf{e}(\boldsymbol{\sigma}) + \mathbf{p}(\boldsymbol{\xi}) \tag{3}$$

where $\mathbf{e}(\boldsymbol{\sigma}) = \mathbf{C}^{-1}\boldsymbol{\sigma}$ is elastic strain tensor; $\boldsymbol{\xi}$ is internal variable and $\mathbf{p}(\boldsymbol{\xi})$ is an irreversible plastic strain in which $\mathbf{C}$ is a fourth order tensor of material constants.

To describe properly the evolution process for the plastic strain, it is required to define the admissible stresses, a yield function, and an associated flow rule. In this work, we use the von-Mises yield function and the Prandtl–Reuss flow rule. Let $\mathbf{p}$ and $\boldsymbol{\xi}$ be the kinematic variables of the generalized strain $\mathbf{P} = (\mathbf{p}, \boldsymbol{\xi})$, and $\boldsymbol{\Sigma} = (\boldsymbol{\sigma}, \boldsymbol{\alpha})$ be the corresponding generalized stress, where $\boldsymbol{\alpha}$ is the hardening parameter describing internal stresses. We define Υ to be the admissible stresses set, which is a closed, convex set, containing 0, and defined by

$$\Upsilon = \{\Sigma : \Phi(\Sigma) \leq 0\} \tag{4}$$

where Φ is the von-Mises yield function which is presented specifically for different visco-elastoplasticity cases as follows:

Case a: Perfect visco-elastoplasticity

In this case, there is no hardening and the internal variables $\boldsymbol{\xi}, \boldsymbol{\alpha}$ are absent. The von-Mises yield function is given simply by

$$\Phi(\boldsymbol{\sigma}) = \|\mathrm{dev}(\boldsymbol{\sigma})\| - \sigma_Y \tag{5}$$

where σ_Y is the yield stress; $\|\mathbf{x}\|$ is the norm of tensor $\mathbf{x}$ and computed by $\|\mathbf{x}\| = \sqrt{\sum_{i=1}^{2}\sum_{j=1}^{2}\mathbf{x}_{ij}^2}$; $\mathrm{dev}(\mathbf{x})$ is the deviator tensor of tensor $\mathbf{x}$ and defined by

$$\mathrm{dev}(\mathbf{x}) = \mathbf{x} - \frac{\mathrm{tr}(\mathbf{x})}{2}\mathbf{I} \tag{6}$$

in which $\mathbf{I}$ is the symmetric unit tensor and $\mathrm{tr}(\mathbf{x}) = \sum_{i=1}^{2} \mathbf{x}_{ii}$ is the trace operator of tensor $\mathbf{x}$.

For the viscosity parameter $v > 0$, the Prandtl–Reuss flow rule has the form

$$\dot{\mathbf{p}} = \begin{cases} \dfrac{1}{v}\left(\|\mathrm{dev}\,(\boldsymbol{\sigma})\| - \sigma_Y\right) & \text{if } \|\mathrm{dev}\,(\boldsymbol{\sigma})\| > \sigma_Y \\ 0 & \text{if } \|\mathrm{dev}\,(\boldsymbol{\sigma})\| \le \sigma_Y \end{cases} \tag{7}$$

Case b: Visco-elastoplasticity with isotropic hardening

In the case of the isotropic hardening, the problem is characterized by a modulus of hardening $H \ge 0$, and $\boldsymbol{\alpha} \equiv \alpha^I \ge 0$ (I means Isotropic) becomes a scalar hardening parameter and relates to the scalar internal strain variable ξ by

$$\alpha^I = -H_1 \xi \tag{8}$$

where H_1 is a positive hardening parameter.

The von-Mises yield function is given by

$$\Phi(\boldsymbol{\sigma}, \alpha^I) = \|\mathrm{dev}(\boldsymbol{\sigma})\| - \sigma_Y(1 + H\alpha^I) \tag{9}$$

For the viscosity parameter $v > 0$, the Prandtl–Reuss flow rule has the form

$$\begin{pmatrix} \dot{\mathbf{p}} \\ \dot{\xi} \end{pmatrix} = \begin{cases} \dfrac{1}{v}\dfrac{1}{\left(1 + H^2\sigma_Y^2\right)} \begin{pmatrix} \|\mathrm{dev}\,(\boldsymbol{\sigma})\| - \left(1+\alpha^I H\right)\sigma_Y \\ -H\sigma_Y\left(\|\mathrm{dev}\,(\boldsymbol{\sigma})\| - \left(1+\alpha^I H\right)\sigma_Y\right) \end{pmatrix} & \text{if } \|\mathrm{dev}\,(\boldsymbol{\sigma})\| > \left(1+\alpha^I H\right)\sigma_Y \\ \begin{pmatrix} 0 \\ 0 \end{pmatrix} & \text{if } \|\mathrm{dev}\,(\boldsymbol{\sigma})\| \le \left(1+\alpha^I H\right)\sigma_Y \end{cases} \tag{10}$$

Case c: Visco-elastoplasticity with linear kinematic hardening

In the case of the linear kinematic hardening, the internal stress $\boldsymbol{\alpha} \equiv \boldsymbol{\alpha}^K$ (K means Kinematic) relates to the internal strain $\boldsymbol{\xi}$ by

$$\boldsymbol{\alpha}^K = -k_1 \boldsymbol{\xi} \tag{11}$$

where k_1 is a positive parameter.

The von-Mises yield function is given by

$$\Phi(\boldsymbol{\sigma}, \boldsymbol{\alpha}^K) = \|\mathrm{dev}(\boldsymbol{\sigma}) - \mathrm{dev}(\boldsymbol{\alpha}^K)\| - \sigma_Y \tag{12}$$

For the viscosity parameter $v > 0$, the Prandtl–Reuss flow rule has the form

$$\begin{pmatrix} \dot{\mathbf{p}} \\ \dot{\xi} \end{pmatrix} = \begin{cases} \dfrac{1}{2v}\begin{pmatrix} \left\|\mathrm{dev}\left(\boldsymbol{\sigma} - \boldsymbol{\alpha}^K\right)\right\| - \sigma_Y \\ -\left(\left\|\mathrm{dev}\left(\boldsymbol{\sigma} - \boldsymbol{\alpha}^K\right)\right\| - \sigma_Y\right) \end{pmatrix} & \text{if } \left\|\mathrm{dev}\left(\boldsymbol{\sigma} - \boldsymbol{\alpha}^K\right)\right\| > \sigma_Y \\ \begin{pmatrix} 0 \\ 0 \end{pmatrix} & \text{if } \left\|\mathrm{dev}\left(\boldsymbol{\sigma} - \boldsymbol{\alpha}^K\right)\right\| \le \sigma_Y \end{cases} \tag{13}$$

In general, the Prandtl–Reuss flow rule, with the viscosity parameter $v > 0$, has the form [2]

$$\begin{bmatrix} \dot{\mathbf{p}} \\ \dot{\boldsymbol{\xi}} \end{bmatrix} = \frac{1}{v}\begin{bmatrix} \boldsymbol{\sigma} - \Pi\boldsymbol{\sigma} \\ \boldsymbol{\alpha} - \Pi\boldsymbol{\alpha} \end{bmatrix} \tag{14}$$

where $\Pi\boldsymbol{\sigma}$ and $\Pi\boldsymbol{\alpha}$ are defined as the projections of $(\boldsymbol{\sigma}, \boldsymbol{\alpha})$ into the admissible stresses set Υ.

The visco-elastoplastic problem can now be stated generally in a weak formulation with the above-mentioned flow rules as follows: Seek $\mathbf{u} \in (\mathbb{H}^1(\Omega))^2$ such that $\mathbf{u} = \mathbf{w}_0$ on Γ_D and $\forall \mathbf{v} \in (\mathbb{H}_0^1(\Omega))^2 = \{\mathbf{v} \in (\mathbb{H}^1(\Omega))^2 : \mathbf{v} = \mathbf{0} \text{ on } \Gamma_D\}$, the following equations are satisfied

$$\int_\Omega \boldsymbol{\sigma}(\mathbf{u}) : \boldsymbol{\varepsilon}(\mathbf{v}) d\Omega = \int_\Omega \mathbf{b} \cdot \mathbf{v} d\Omega + \int_{\Gamma_N} \bar{\mathbf{t}} \cdot \mathbf{v} d\Gamma \tag{15}$$

$$\begin{bmatrix} \dot{\mathbf{p}} \\ \dot{\boldsymbol{\xi}} \end{bmatrix} = \begin{bmatrix} \boldsymbol{\varepsilon}(\dot{\mathbf{u}}) - \mathbf{C}^{-1}\dot{\sigma} \\ \boldsymbol{\xi}(\dot{\alpha}) \end{bmatrix} = \frac{1}{v}\begin{bmatrix} \boldsymbol{\sigma} - \Pi\boldsymbol{\sigma} \\ \boldsymbol{\alpha} - \Pi\boldsymbol{\alpha} \end{bmatrix} \tag{16}$$

where $\mathbf{A} : \mathbf{B} = \sum_{j,k} \mathbf{A}_{jk}\mathbf{B}_{jk}$ denotes the scalar products of (symmetric) matrices.

2.2 Time discretization scheme

A generalized midpoint rule is used as the time-discretization scheme [2]. In each time step, a spatial problem needs to be solved with given variables $(\mathbf{u}(t), \boldsymbol{\sigma}(t), \boldsymbol{\alpha}(t))$ at time t_0 denoted as $(\mathbf{u}_0, \boldsymbol{\sigma}_0, \boldsymbol{\alpha}_0)$ and unknowns at time $t_1 = t_0 + \Delta t$ denoted as $(\mathbf{u}_1, \boldsymbol{\sigma}_1, \boldsymbol{\alpha}_1)$. Time derivatives are substituted by backward difference quotients; for instance $\dot{\mathbf{u}}$ is substituted by $\frac{\mathbf{u}_\vartheta - \mathbf{u}_0}{\vartheta\,\Delta t}$ where $\mathbf{u}_\vartheta = (1-\vartheta)\mathbf{u}_0 + \vartheta\mathbf{u}_1$ with $1/2 \le \vartheta \le 1$. The time discrete problem now becomes: Seek $\mathbf{u}_\vartheta \in (\mathbb{H}^1(\Omega))^2$ that satisfies $\mathbf{u}_\vartheta = \mathbf{w}_0$ on Γ_D and for $\forall \mathbf{v} \in (\mathbb{H}_0^1(\Omega))^2$

$$\int_\Omega \boldsymbol{\sigma}(\mathbf{u}_\vartheta) : \boldsymbol{\varepsilon}(\mathbf{v}) d\Omega = \int_\Omega \mathbf{b}_\vartheta \cdot \mathbf{v} d\Omega + \int_{\Gamma_N} \bar{\mathbf{t}}_\vartheta \cdot \mathbf{v} d\Gamma \tag{17}$$

$$\frac{1}{\vartheta\,\Delta t}\begin{bmatrix} \boldsymbol{\varepsilon}(\mathbf{u}_\vartheta - \mathbf{u}_0) - \mathbf{C}^{-1}(\boldsymbol{\sigma}_\vartheta - \boldsymbol{\sigma}_0) \\ \boldsymbol{\xi}(\boldsymbol{\alpha}, t_\vartheta) - \boldsymbol{\xi}(\boldsymbol{\alpha}, t_0) \end{bmatrix} = \frac{1}{v}\begin{bmatrix} \boldsymbol{\sigma}_\vartheta - \Pi\boldsymbol{\sigma}_\vartheta \\ \boldsymbol{\alpha}_\vartheta - \Pi\boldsymbol{\alpha}_\vartheta \end{bmatrix} \tag{18}$$

where $\mathbf{b}_\vartheta = (1-\vartheta)\mathbf{b}_0 + \vartheta\mathbf{b}_1, \bar{\mathbf{t}}_\vartheta = (1-\vartheta)\bar{\mathbf{t}}_0 + \vartheta\bar{\mathbf{t}}_1$ in which $\mathbf{b}_0$, $\bar{\mathbf{t}}_0$, $\mathbf{b}_1$ and $\bar{\mathbf{t}}_1$ are body forces and surface forces at time t_0, t_1, respectively.

Equations (17) and (18) is in fact a dual model that has both stress and displacement as field variables. To solve the set of Eqs. (17) and (18) efficiently, we need to eliminate

one variable. This can be done by first expressing explicitly the stress $\boldsymbol{\sigma}_\vartheta$ in the form of displacement $\mathbf{u}_\vartheta$ using Eq. (18), and then substituting it into Eq. (17). The problem will then becomes only displacement-dependent, and we need to solve the resultant form of Eq. (17).

2.3 Analytic expression of the stress tensor

Explicit expressions for the stress tensor $\boldsymbol{\sigma}_\vartheta$ in different cases of visco-elastoplasticity can be presented briefly as follows [2]:

(a) Perfect visco-elastoplasticity
In the elastic phase

$$\boldsymbol{\sigma}_\vartheta = C_1 \mathrm{tr}\,(\vartheta\,\Delta t\mathbf{A})\,\mathbf{I} + 2\mu \mathrm{dev}\,(\vartheta\,\Delta t\mathbf{A}) \tag{19}$$

where $\mathbf{A} = \frac{\boldsymbol{\varepsilon}(\mathbf{u}_\vartheta - \mathbf{u}_0)}{\vartheta\,\Delta t} + \mathbf{C}^{-1}\frac{\boldsymbol{\sigma}_0}{\vartheta\,\Delta t}$.
In the plastic phase, the plastic occurs when $\|\,\mathrm{dev}(\vartheta\,\Delta t\mathbf{A})\| > \beta\sigma_Y$ and

$$\begin{aligned}\boldsymbol{\sigma}_\vartheta &= C_1 \mathrm{tr}(\vartheta\,\Delta t\mathbf{A})\mathbf{I} \\ &\quad + (C_2 + C_3/\|\mathrm{dev}(\vartheta\,\Delta t\mathbf{A})\|)\mathrm{dev}(\vartheta\,\Delta t\mathbf{A}).\end{aligned} \tag{20}$$

where

$$\begin{aligned}&C_1 = \lambda + \mu,\ C_2 = v/(\beta v + \vartheta\,\Delta t),\\ &C_3 = \vartheta\,\Delta t\sigma_Y/(\beta v + \vartheta\,\Delta t)\end{aligned} \tag{21}$$

in which $\beta = 1/(2\mu)$.

(b) Visco-elastoplasticity with isotropic hardening
In the elastic phase

$$\boldsymbol{\sigma}_\vartheta = C_1 \mathrm{tr}(\vartheta\,\Delta t\mathbf{A})\mathbf{I} + 2\mu \mathrm{dev}(\vartheta\,\Delta t\mathbf{A}) \tag{22}$$

In the plastic phase, the plastic occurs when $\|\mathrm{dev}(\vartheta\,\Delta t\mathbf{A})\| > \beta(1 + \alpha_0^I H)\sigma_Y$ and

$$\begin{aligned}\boldsymbol{\sigma}_\vartheta &= C_1 \mathrm{tr}(\vartheta\,\Delta t\mathbf{A})\mathbf{I} + (C_3/(C_2\|\mathrm{dev}(\vartheta\,\Delta t\mathbf{A})\|) \\ &\quad + C_4/C_2)\mathrm{dev}(\vartheta\,\Delta t\mathbf{A})\end{aligned} \tag{23}$$

where

$$\begin{aligned}&C_1 = \lambda + \mu,\\ &C_2 = \beta v(1 + H^2\sigma_Y^2) + \vartheta\,\Delta t(1 + \beta H_1 H^2\sigma_Y^2)\\ &C_3 = \vartheta\,\Delta t\sigma_Y(1 + \alpha_0^I H),\\ &C_4 = H_1 H^2\vartheta\,\Delta t\sigma_Y^2 + v(1 + H^2\sigma_Y^2)\end{aligned} \tag{24}$$

in which α_0^I is the initial scalar hardening parameter.
(c) Visco-elastoplasticity with linear kinematic hardening
In the elastic phase

$$\boldsymbol{\sigma}_\vartheta = C_1 \mathrm{tr}(\vartheta\,\Delta t\mathbf{A})\mathbf{I} + 2\mu \mathrm{dev}(\vartheta\,\Delta t\mathbf{A}) \tag{25}$$

In the plastic phase, the plastic occurs when $\|\mathrm{dev}(\vartheta\,\Delta t\mathbf{A} - \beta\boldsymbol{\alpha}_0^K)\| > \beta\sigma_Y$ and

$$\begin{aligned}\boldsymbol{\sigma}_\vartheta &= C_1 \mathrm{tr}(\vartheta\,\Delta t\mathbf{A})\mathbf{I} \\ &\quad + (C_2 + C_3/\|\mathrm{dev}(\vartheta\,\Delta t\mathbf{A} - \beta\boldsymbol{\alpha}_0^K)\|) \\ &\quad \times \mathrm{dev}(\vartheta\,\Delta t\mathbf{A} - \beta\boldsymbol{\alpha}_0^K) + \mathrm{dev}(\boldsymbol{\alpha}_0^K)\end{aligned} \tag{26}$$

where

$$\begin{aligned}&C_1 = \lambda + \mu,\quad C_2 = \frac{\vartheta\,\Delta t k_1 + 2v}{\vartheta\,\Delta t + \beta\vartheta\,\Delta t k_1 + v/\mu},\\ &C_3 = \frac{\vartheta\,\Delta t\sigma_Y}{\vartheta\,\Delta t + \beta\vartheta\,\Delta t k_1 + v/\mu}\end{aligned} \tag{27}$$

Now, by replacing the stress $\boldsymbol{\sigma}_\vartheta$ described explicitly into Eq. (17), we obtain the only displacement-dependent problem and can apply different numerical methods to solve.

2.4 Discretization in space using the FEM

The domain Ω is now discretized into N_e elements and N_n nodes such that $\Omega = \bigcup_{e=1}^{N_e}\Omega_e$ and $\Omega_i \cap \Omega_j = \varnothing, i \neq j$. In the discrete version of (17), the spaces $\mathbb{V} = (\mathbb{H}^1(\Omega))^2$ and $\mathbb{V}_0 = (\mathbb{H}_0^1(\Omega))^2$ are replaced by finite dimensional subspaces $\mathbb{V}^h \subset \mathbb{V}$ and $\mathbb{V}_0^h \subset \mathbb{V}_0$. The discrete problem now becomes: Seek $\mathbf{u}_\vartheta \in \mathbb{V}^h$ such that $\mathbf{u}_\vartheta = \mathbf{w}_0$ on Γ_D and

$$\begin{aligned}&\int_\Omega \boldsymbol{\sigma}_\vartheta\left(\boldsymbol{\varepsilon}\,(\mathbf{u}_\vartheta - \mathbf{u}_0) + \mathbf{C}^{-1}\boldsymbol{\sigma}_0\right) : \boldsymbol{\varepsilon}(\mathbf{v})d\Omega\\ &= \int_\Omega \mathbf{b}_\vartheta \cdot \mathbf{v}d\Omega + \int_{\Gamma_N} \bar{\mathbf{t}}_\vartheta \cdot \mathbf{v}d\Gamma \quad \text{for} \quad \forall\mathbf{v} \in \mathbb{V}_0^h\end{aligned} \tag{28}$$

Let $(\varphi_1, \ldots, \varphi_{2N_n})$ be the nodal basis of the finite dimensional space $\mathbb{V}^h$, where φ_i is the independent scalar hat shape function on node satisfying condition Kronecker $\varphi_i(i) = 1$ and $\varphi_i(j) = 0, i \neq j$, then Eq. (28) now becomes: seeking $\mathbf{u}_\vartheta \in \mathbb{V}^h$ such that

$$\begin{aligned}\mathbf{F}_i &= \int_\Omega \boldsymbol{\sigma}_\vartheta\left(\boldsymbol{\varepsilon}\,(\mathbf{u}_\vartheta - \mathbf{u}_0) + \mathbf{C}^{-1}\boldsymbol{\sigma}_0\right) : \boldsymbol{\varepsilon}(\varphi_i)d\Omega\\ &\quad - \int_\Omega \mathbf{b}_\vartheta \cdot \varphi_i d\Omega - \int_{\Gamma_N} \bar{\mathbf{t}}_\vartheta \cdot \varphi_i d\Gamma = 0\end{aligned} \tag{29}$$

for $i = 1, \ldots, 2N_n$. $\mathbf{F}_i$ in Eq. (29) can be written in the sum of a part $\mathbf{Q}_i$ which depends on $\mathbf{u}_\vartheta$ and a part $\mathbf{P}_i$ which is independent of $\mathbf{u}_\vartheta$ such as

$$\mathbf{F}_i(\mathbf{u}_\vartheta) = \mathbf{Q}_i(\mathbf{u}_\vartheta) - \mathbf{P}_i \tag{30}$$

with

$$\mathbf{Q}_i(\mathbf{u}_\vartheta) = \mathbf{Q}_i = \int_\Omega \boldsymbol{\sigma}_\vartheta \left(\boldsymbol{\varepsilon}(\mathbf{u}_\vartheta - \mathbf{u}_0) + \mathbf{C}^{-1}\boldsymbol{\sigma}_0\right) : \boldsymbol{\varepsilon}(\varphi_i) d\Omega \tag{31}$$

$$\mathbf{P}_i = \int_\Omega \mathbf{b}_\vartheta \cdot \varphi_i d\Omega + \int_{\Gamma_N} \bar{\mathbf{t}}_\vartheta \cdot \varphi_i d\Gamma \tag{32}$$

2.5 Iterative solution

In order to solve Eq. (29) in this work, Newton–Raphson method is used [2]. In each step of the Newton iterations, the discrete displacement vector $\mathbf{u}_\vartheta^p$ expressed in the nodal basis by $\mathbf{u}_\vartheta^p = \sum_{i=1}^{2N_n} \varphi_i u_i$ is determined from iterative solution

$$\mathbf{DF}(\mathbf{u}_\vartheta^p)\mathbf{u}_\vartheta^{p+1} = \mathbf{DF}(\mathbf{u}_\vartheta^p)\mathbf{u}_\vartheta^p - \mathbf{F}(\mathbf{u}_\vartheta^p) \tag{33}$$

where **DF** is in fact the system stiffness matrix whose the local entries are defined as

$$\left(\mathbf{DF}\left(u^p_{\vartheta,1}, \ldots, u^p_{\vartheta,2N_n}\right)\right)_{rs} = \partial \mathbf{F}_r \left(u^p_{\vartheta,1}, \ldots, u^p_{\vartheta,2N_n}\right) \Big/ \partial u^p_{\vartheta,s} \tag{34}$$

where $r, s \in \Psi_{\text{dof}}$ which is the set containing degrees of freedom of all the nodes.

To properly apply the Dirichlet boundary conditions for our nonlinear problem, we use the approach of Lagrange multipliers. Combining the Newton iteration (33) and the set of boundary conditions imposed through Lagrange multipliers $\boldsymbol{\lambda}$, the extended system of equations is obtained

$$\begin{pmatrix} \mathbf{DF}(\mathbf{u}_\vartheta^p) & \mathbf{G}^T \\ \mathbf{G} & 0 \end{pmatrix} \begin{pmatrix} \mathbf{u}_\vartheta^{p+1} \\ \boldsymbol{\lambda} \end{pmatrix} = \begin{pmatrix} \mathbf{f} \\ \mathbf{w}_0 \end{pmatrix} \tag{35}$$

with $\mathbf{f} = \mathbf{DF}(\mathbf{u}_\vartheta^p)\mathbf{u}_\vartheta^p - \mathbf{F}(\mathbf{u}_\vartheta^p)$ and $\mathbf{G}$ is a matrix created from Dirichlet boundary conditions such that $\mathbf{G}\mathbf{u}_\vartheta^{p+1} = \mathbf{w}_0$.

The extended system of equations (35) can now be solved for $\mathbf{u}_\vartheta^{p+1}$ and $\boldsymbol{\lambda}$ at each time step. The solving process is iterated until the relative residual $\mathbf{F}(u^{p+1}_{\vartheta,z_1}, \ldots, u^{p+1}_{\vartheta,z_m})$ for the m free nodes $(z_1, \ldots, z_m) \in \Xi$ (where Ξ is the set of free nodes) is smaller than a given tolerance or the maximum number of iterations is larger than a prescribed number.

2.6 Discretization in space using the ES-FEM

In the ES-FEM, the domain discretization is still based on the triangulation using triangular elements as in the standard FEM, but the integration required in the weak form (29) is performed based on the "smoothing domains" associated with the edges, and strain smoothing technique [4] is used. In such an integration process, the closed problem domain Ω is divided into $N_{SD} = N_{ed}$ smoothing domains associated with edges such that $\Omega = \sum_{k=1}^{N_{ed}} \Omega^{(k)}$ and $\Omega^{(i)} \cap \Omega^{(j)} = \varnothing$, $i \neq j$, in which N_{ed} is the total number of edges located in the entire problem domain. For triangular elements, the smoothing domain $\Omega^{(k)}$ associated with the edge k is created by connecting two endpoints of the edge to centroids of adjacent elements as shown in Fig. 3.

Using the edge-based smoothing domains, smoothed strains $\tilde{\boldsymbol{\varepsilon}}_k$ can now be obtained using the *compatible* strains $\boldsymbol{\varepsilon}^h = \nabla_s \mathbf{u}_\vartheta$ through the following smoothing operation over domain $\Omega^{(k)}$ associated with edge k

$$\tilde{\boldsymbol{\varepsilon}}_k = \int_{\Omega^{(k)}} \boldsymbol{\varepsilon}^h(\mathbf{x})\Phi_k(\mathbf{x}) d\Omega = \int_{\Omega^{(k)}} \nabla_s \mathbf{u}_\vartheta(\mathbf{x})\Phi_k(\mathbf{x}) d\Omega \tag{36}$$

where $\Phi_k(\mathbf{x})$ is a given smoothing function that satisfies at least unity property

$$\int_{\Omega^{(k)}} \Phi_k(\mathbf{x}) d\Omega = 1 \tag{37}$$

In the ES-FEM [14], we use the simplest local constant smoothing function

$$\Phi_k(\mathbf{x}) = \begin{cases} 1/A^{(k)} & \mathbf{x} \in \Omega^{(k)} \\ 0 & \mathbf{x} \notin \Omega^{(k)} \end{cases} \tag{38}$$

where $A^{(k)}$ is the area of the smoothing domain $\Omega^{(k)}$ and is calculated by

$$A^{(k)} = \int_{\Omega^{(k)}} d\Omega = \frac{1}{3}\sum_{j=1}^{N_e^{(k)}} A_e^{(j)} \tag{39}$$

where $N_e^{(k)}$ is the number of elements around the edge k ($N_e^{(k)} = 1$ for the boundary edges and $N_e^{(k)} = 2$ for inner edges as shown in Fig. 3) and $A_e^{(j)}$ is the area of the jth element around the edge k.

In the ES-FEM, the trial function is similar as in the standard FEM with

$$\mathbf{u}_\vartheta^p = \sum_{i=1}^{2N_n} \varphi_i u_i \tag{40}$$

Substituting Eqs. (40) and (38) into (36), the smoothed strain on the domain $\Omega^{(k)}$ associated with edge k can be written in the following matrix form of nodal displacements

$$\tilde{\boldsymbol{\varepsilon}}_k = \sum_{I \in \Psi_{\text{dof}}^{(k)}} \tilde{\mathbf{B}}_I(\mathbf{x}_k) u_I \tag{41}$$

where $\Psi_{\text{dof}}^{(k)}$ is the set containing degrees of freedom of elements attached to the common edge k (for example, for the boundary edge m as presented in Fig. 3, $\Psi_{\text{dof}}^{(k)}$ is the set

containing degrees of freedom of nodes $\{A,\ B,\ C\}$ and the total number of degrees of freedom $N_{\text{dof}}^{(k)} = 6$; for the inner edge k as presented in Fig. 3, $\Psi_{\text{dof}}^{(k)}$ is the set containing degrees of freedom of nodes $\{D,\ E,\ F,\ G\}$ and the total number of degrees of freedom $N_{\text{dof}}^{(k)} = 8$) and $\tilde{\mathbf{B}}_I(\mathbf{x}_k)$, that is termed as the *smoothed strain matrix* on the domain $\Omega^{(k)}$, is calculated numerically by an assembly process similarly as in FEM

$$\tilde{\mathbf{B}}_I(\mathbf{x}_k) = \frac{1}{A^{(k)}} \sum_{j=1}^{N_e^{(k)}} \frac{1}{3} A_e^{(j)} \mathbf{B}_j \tag{42}$$

where $\mathbf{B}_j$ is the strain gradient matrix of the jth element around the edge k which has the following form in the 2D linear elastic problems

$$\mathbf{B}_j = \begin{bmatrix} \varphi_{j,x} & 0 \\ 0 & \varphi_{j,y} \\ \varphi_{j,y} & \varphi_{j,x} \end{bmatrix} \tag{43}$$

Due to the use of the triangular elements with the linear shape functions, the entries of matrix $\mathbf{B}_j$ are constants, and so are the entries of matrix $\tilde{\mathbf{B}}_I(\mathbf{x}_k)$. Note that with this formulation, only the area and the usual compatible strain gradient matrices $\mathbf{B}_j$ of triangular elements are needed to calculate the system stiffness matrix for ES-FEM. This formulation is quite straightforward to extend for the 3D problems using tetrahedral elements [21,23].

In the discrete version of the visco-elastoplastic problems using the ES-FEM with the smoothed strain (36) used for smoothing domains associated with edges, Eq. (29) now becomes: seeking $\mathbf{u}_\vartheta \in \mathbb{V}^h$ such that

$$\mathbf{F}_i = \int_\Omega \boldsymbol{\sigma}_\vartheta \left(\tilde{\boldsymbol{\varepsilon}} (\mathbf{u}_\vartheta - \mathbf{u}_0) + \mathbf{C}^{-1} \boldsymbol{\sigma}_0 \right) : \tilde{\boldsymbol{\varepsilon}}(\varphi_i) d\Omega - \int_\Omega \mathbf{b}_\vartheta \cdot \varphi_i d\Omega - \int_{\Gamma_N} \bar{\mathbf{t}}_\vartheta \cdot \varphi_i d\Gamma = 0 \tag{44}$$

for $i = 1, \ldots, 2N_n$, and the local stiffness matrix $\mathbf{DF}_{rs}^{(k)}$ in Eq. (34) associated with smoothing domain $\Omega^{(k)}$ can be expressed as follows

$$\begin{aligned} \mathbf{DF}_{rs}^{(k)} &= \frac{\partial \mathbf{F}_r^{(k)}}{\partial u_{\vartheta,s}^p} = \frac{\partial \mathbf{Q}_r^{(k)}}{\partial u_{\vartheta,s}^p} \\ &= \frac{\partial}{\partial u_{\vartheta,s}^p} \left(\int_{\Omega^{(k)}} \boldsymbol{\sigma}_\vartheta \left(\tilde{\boldsymbol{\varepsilon}}_k \left(\sum_{l \in \Psi_{\text{dof}}^{(k)}} u_{\vartheta,l}^p \varphi_l - \mathbf{u}_0 \right) + \mathbf{C}^{-1} \boldsymbol{\sigma}_0 \right) : \tilde{\boldsymbol{\varepsilon}}_k(\varphi_r) d\Omega \right) \end{aligned} \tag{45}$$

where $r, s \in \Psi_{\text{dof}}^{(k)}$, and

$$\mathbf{Q}_r^{(k)} = \int_{\Omega^{(k)}} \boldsymbol{\sigma}_\vartheta \left(\tilde{\boldsymbol{\varepsilon}}_k (\mathbf{u}_\vartheta - \mathbf{u}_0) + \mathbf{C}^{-1} \boldsymbol{\sigma}_0 \right) : \tilde{\boldsymbol{\varepsilon}}_k(\varphi_r) d\Omega \tag{46}$$

The expression $\boldsymbol{\sigma}_\vartheta (\tilde{\boldsymbol{\varepsilon}}_k(\mathbf{u}_\vartheta - \mathbf{u}_0) + \mathbf{C}^{-1}\boldsymbol{\sigma}_0)$ in Eqs. (45) and (46) now is replaced by $\boldsymbol{\sigma}_\vartheta$ written explicitly in Eqs. (19), (20), (22), (23), (25), (26) for different cases of visco-elastoplasticity with just replacing $\boldsymbol{\varepsilon}$ by $\tilde{\boldsymbol{\varepsilon}}_k$ in corresponding positions which give the following results:

(a) Visco-elastoplasticity:

$$\begin{aligned} \mathbf{Q}_r^{(k)} &= A^{(k)} \left(C_1 \text{tr}(\tilde{\mathbf{v}}_k) \text{tr} \left(\tilde{\boldsymbol{\varepsilon}}_k(\varphi_r) \right) \right. \\ &\quad \left. + C_4 \text{dev}(\tilde{\mathbf{v}}_k) : \tilde{\boldsymbol{\varepsilon}}_k(\varphi_r) \right) \end{aligned} \tag{47}$$

$$\begin{aligned} \mathbf{DF}_{rs}^{(k)} &= A^{(k)} \left(C_1 \text{tr} \left(\tilde{\boldsymbol{\varepsilon}}_k(\varphi_r) \right) \text{tr} \left(\tilde{\boldsymbol{\varepsilon}}_k(\varphi_s) \right) \right. \\ &\quad + C_4 \text{dev} \left(\tilde{\boldsymbol{\varepsilon}}_k(\varphi_r) \right) : \tilde{\boldsymbol{\varepsilon}}_k(\varphi_s) \\ &\quad \left. - (C_5)_r \text{dev}(\tilde{\mathbf{v}}_k) : \tilde{\boldsymbol{\varepsilon}}_k(\varphi_s) \right) \end{aligned} \tag{48}$$

where $\tilde{\mathbf{v}}_k = \tilde{\boldsymbol{\varepsilon}}_k(\mathbf{u}_\vartheta - \mathbf{u}_0) + \mathbf{C}^{-1}\boldsymbol{\sigma}_0$ and

$$C_4 = \begin{cases} C_2 + C_3 / \|\text{dev}(\tilde{\mathbf{v}}_k)\| & \text{if } \|\text{dev}(\tilde{\mathbf{v}}_k)\| - \beta\sigma_Y > 0 \\ 2\mu & \text{else} \end{cases}$$

$$C_5 = \begin{cases} C_3 / \|\text{dev}(\tilde{\mathbf{v}}_k)\|^3 \left[\text{dev} \left(\tilde{\boldsymbol{\varepsilon}}_k(\varphi_r) \right) : \text{dev}(\tilde{\mathbf{v}}_k) \right]_{r=1}^{N_{\text{dof}}^{(k)}} & \text{if } \|\text{dev}(\tilde{\mathbf{v}}_k)\| - \beta\sigma_Y > 0 \\ \underbrace{\left[0 \cdots 0 \right]^T}_{\text{size of } 1 \times N_{\text{dof}}^{(k)}} & \text{else} \end{cases} \tag{49}$$

in which C_1, C_2, C_3 are determined by (21).

(b) Visco-elastoplasticity with isotropic hardening

$$\begin{aligned} \mathbf{Q}_r^{(k)} &= A^{(k)} \left(C_1 \text{tr}(\tilde{\mathbf{v}}_k) \text{tr} \left(\tilde{\boldsymbol{\varepsilon}}_k(\varphi_r) \right) \right. \\ &\quad \left. + C_5 \text{dev}(\tilde{\mathbf{v}}_k) : \tilde{\boldsymbol{\varepsilon}}_k(\varphi_r) \right) \end{aligned} \tag{50}$$

$$\begin{aligned} \mathbf{DF}_{rs}^{(k)} &= A^{(k)} \left(C_1 \text{tr} \left(\tilde{\boldsymbol{\varepsilon}}_k(\varphi_r) \right) \text{tr} \left(\tilde{\boldsymbol{\varepsilon}}_k(\varphi_s) \right) \right. \\ &\quad + C_5 \text{dev} \left(\tilde{\boldsymbol{\varepsilon}}_k(\varphi_r) \right) : \tilde{\boldsymbol{\varepsilon}}_k(\varphi_s) \\ &\quad \left. - (C_6)_r \text{dev}(\tilde{\mathbf{v}}_k) : \tilde{\boldsymbol{\varepsilon}}_k(\varphi_s) \right) \end{aligned} \tag{51}$$

where

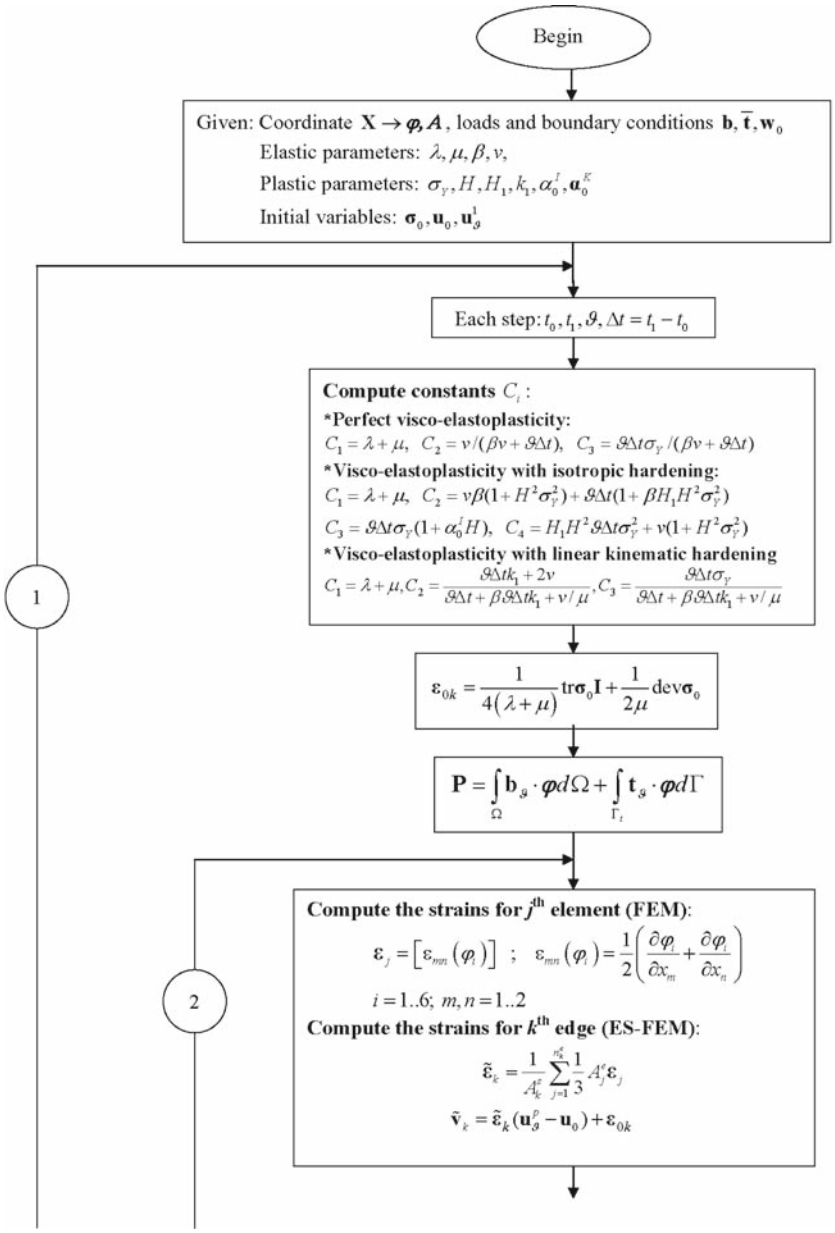

Fig. 4 Flow chart to solve the visco-elastoplastic problems using the ES-FEM: part 1

$$C_5 = \begin{cases} C_3/\left(C_2\left\|\mathrm{dev}(\tilde{\mathbf{v}}_k)\right\|\right) + C_4/C_2 & \text{if } \left\|\mathrm{dev}(\tilde{\mathbf{v}}_k)\right\| - \beta\left(1+\alpha_0^I H\right)\sigma_Y > 0 \\ 2\mu & \text{else} \end{cases}$$

$$C_6 = \begin{cases} C_3/\left(C_2\left\|\mathrm{dev}(\tilde{\mathbf{v}}_k)\right\|^3\right)\left[\mathrm{dev}\left(\tilde{\boldsymbol{\varepsilon}}_k(\varphi_r)\right) : \mathrm{dev}(\tilde{\mathbf{v}}_k)\right]_{r=1}^{N_{\text{dof}}^{(k)}} & \text{if } \left\|\mathrm{dev}(\tilde{\mathbf{v}}_k)\right\| - \beta\left(1+\alpha_0^I H\right)\sigma_Y > 0 \\ \underbrace{\left[0 \cdots 0\right]^T}_{\text{size of } 1\times N_{\text{dof}}^{(k)}} & \text{else} \end{cases} \tag{52}$$

in which C_1, C_2, C_3, C_4 is determined by (24).

(c) Visco-elastoplasticity with linear kinematic hardening

$$\mathbf{Q}_r^{(k)} = A^{(k)}\Big(C_1\mathrm{tr}(\tilde{\mathbf{v}}_k)\mathrm{tr}\left(\tilde{\boldsymbol{\varepsilon}}_k(\varphi_r)\right) + C_4\mathrm{dev}(\tilde{\mathbf{v}}_k) : \tilde{\boldsymbol{\varepsilon}}_k(\varphi_r) + c\,\mathrm{dev}(\boldsymbol{\alpha}_0^K) : \tilde{\boldsymbol{\varepsilon}}_k(\varphi_r)\Big) \tag{53}$$

$$\mathbf{DF}_{rs}^{(k)} = A^{(k)}\left(C_1\mathrm{tr}\left(\tilde{\boldsymbol{\varepsilon}}_k(\varphi_r)\right)\mathrm{tr}\left(\tilde{\boldsymbol{\varepsilon}}_k(\varphi_s)\right) + C_4\mathrm{dev}\left(\tilde{\boldsymbol{\varepsilon}}_k(\varphi_r)\right) : \tilde{\boldsymbol{\varepsilon}}_k(\varphi_s) - (C_5)_r\mathrm{dev}(\tilde{\mathbf{v}}_k) : \tilde{\boldsymbol{\varepsilon}}_k(\varphi_s)\right) \tag{54}$$

where

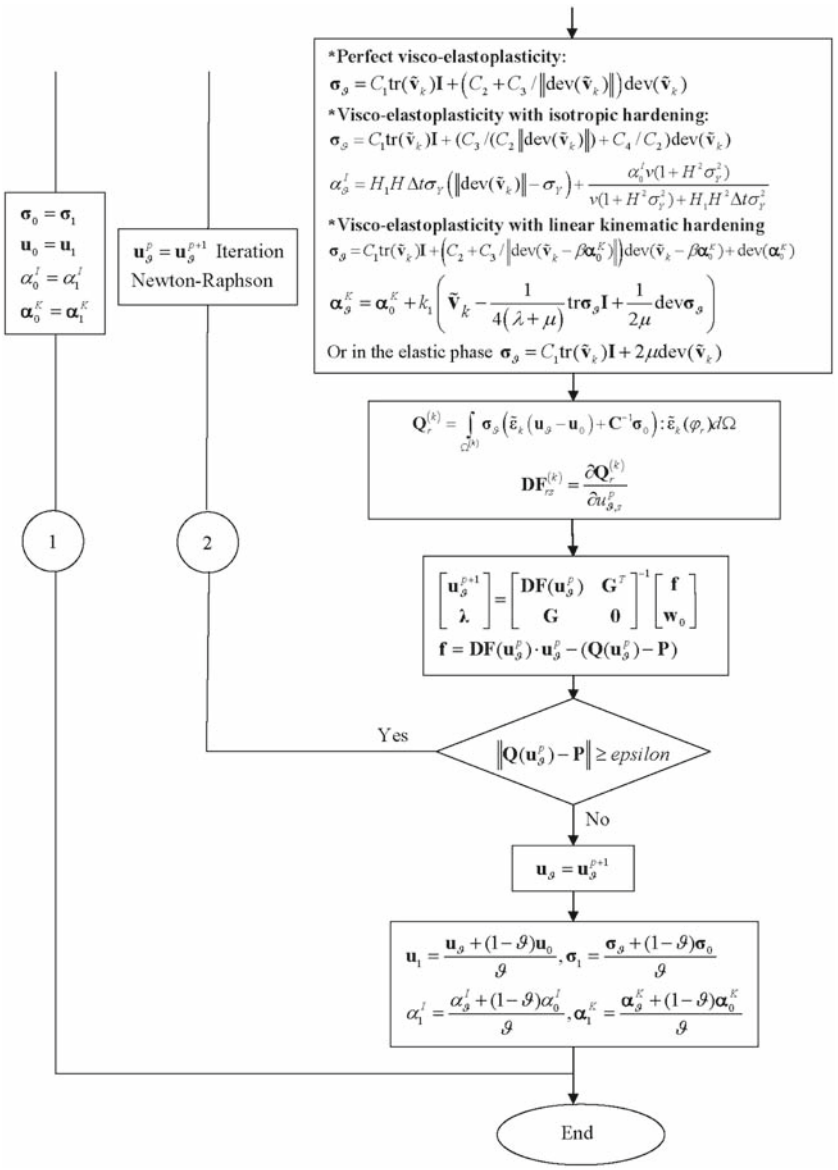

Fig. 5 Flow chart to solve the visco-elastoplastic problems using the ES-FEM: part 2

$$C_4 = \begin{cases} C_3/\|\mathrm{dev}(\tilde{\mathbf{v}}_k)\| + C_2 & \text{if } \left\|\mathrm{dev}\left(\tilde{\mathbf{v}}_k - \beta\boldsymbol{\alpha}_0^K\right)\right\| - \beta\sigma_Y > 0 \\ 2\mu & \text{else} \end{cases} \tag{55}$$

$$C_5 = \begin{cases} C_3/\|\mathrm{dev}(\tilde{\mathbf{v}}_k)\|^3 \left[\mathrm{dev}\left(\tilde{\boldsymbol{\varepsilon}}_k(\varphi_r)\right) : \mathrm{dev}(\tilde{\mathbf{v}}_k)\right]_{r=1}^{N_{\mathrm{dof}}^{(k)}} & \text{if } \left\|\mathrm{dev}\left(\tilde{\mathbf{v}}_k - \beta\boldsymbol{\alpha}_0^K\right)\right\| - \beta\sigma_Y > 0 \\ \underbrace{\left[0 \cdots 0\right]^T}_{\text{size of } 1\times N_{\mathrm{dof}}^{(k)}} & \text{else} \end{cases}$$

$$c = \begin{cases} 1 & \text{if } \left\|\mathrm{dev}\left(\tilde{\mathbf{v}}_k - \beta\boldsymbol{\alpha}_0^K\right)\right\| - \beta\sigma_Y > 0 \\ 0 & \text{else} \end{cases}$$

in which C_1, C_2, C_3 is determined by (27).

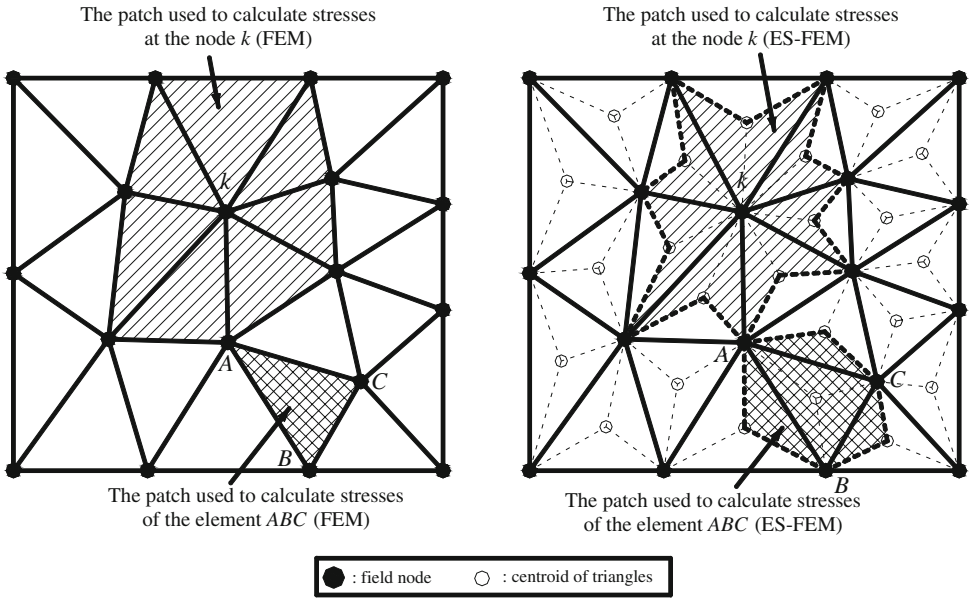

Fig. 6 Patches used to calculate stresses of the nodes and the elements of two methods FEM and ES-FEM

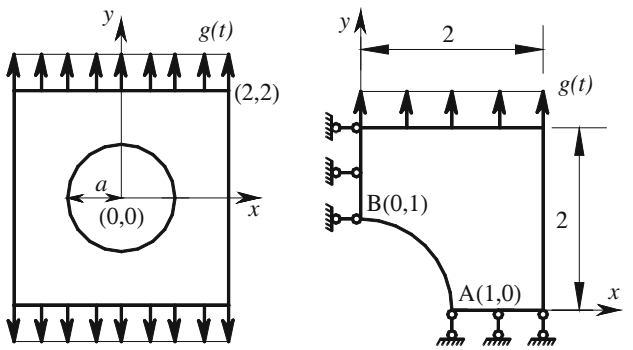

Fig. 7 Plate with a circular hole subjected to time dependent surface forces $g(t)$ and its quarter model with symmetric conditions imposed on the left and bottom edges

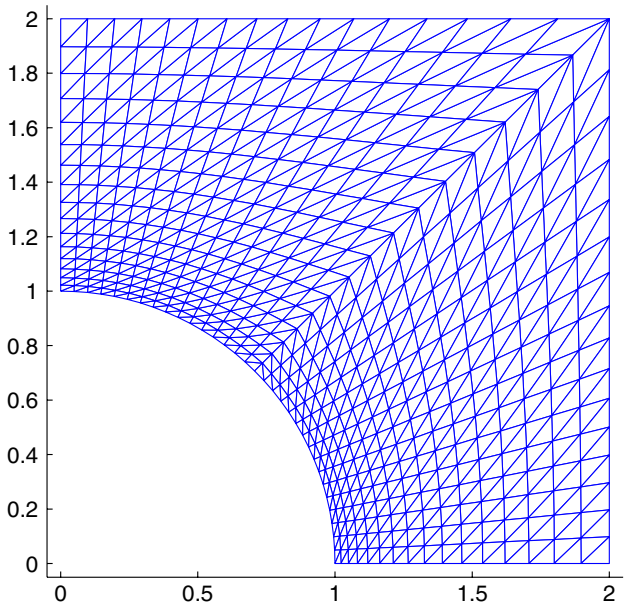

Fig. 8 A domain discretization using 561 nodes and 1,024 triangular elements for the plate with a circular hole subjected to time dependent surface forces $g(t)$

Applying the Dirichlet boundary conditions and solving the extended system of equations (35) by the ES-FEM are identical to those of the FEM.

Recall one disadvantage of the ES-FEM is that the bandwidth of stiffness matrix is larger than that of the FEM, because the number of nodes related to the smoothing domains associated with inner edges is 4, which is 1 larger than that related to the elements. The computational cost of the ES-FEM therefore is larger than that of FEM for the same meshes. We also note that the trial function $\mathbf{u}_{\vartheta}(\mathbf{x})$ for elements in the ES-FEM is the same as in the standard FEM and therefore the force vector $\mathbf{P}_i$ in the ES-FEM is computed in the same way as in the FEM. In other words, the ES-FEM changes only the stiffness matrix. Figures 4 and 5 present the flow chart to solve the visco-elastoplastic problems using the ES-FEM.

3 A-posteriori error estimation

In order to estimate the accuracy of the ES-FEM compared to the FEM for the visco-elastoplastic problems, in this work

Table 1 Number of iterations and the estimated error using the FEM and ES-FEM at various time steps for the plate with hole

Step	FEM		ES-FEM	
	Iterations	$\eta^h = \frac{\|\mathbf{R}\boldsymbol{\sigma}^h - \boldsymbol{\sigma}^h\|_{L_2(\Omega)}}{\|\boldsymbol{\sigma}^h\|_{L_2(\Omega)}}$	Iterations	$\eta^h = \frac{\|\mathbf{R}\boldsymbol{\sigma}^h - \boldsymbol{\sigma}^h\|_{L_2(\Omega)}}{\|\boldsymbol{\sigma}^h\|_{L_2(\Omega)}}$
1	1	0.1	1	0.0475
2	1	0.1	1	0.0475
3	1	0.1	1	0.0475
4	1	0.1	1	0.0475
5	1	0.1	1	0.0475
6	1	0.1	1	0.0475
7	3	0.1	3	0.0475
8	4	0.101	4	0.0476
9	4	0.103	4	0.0480
10	4	0.106	4	0.0486

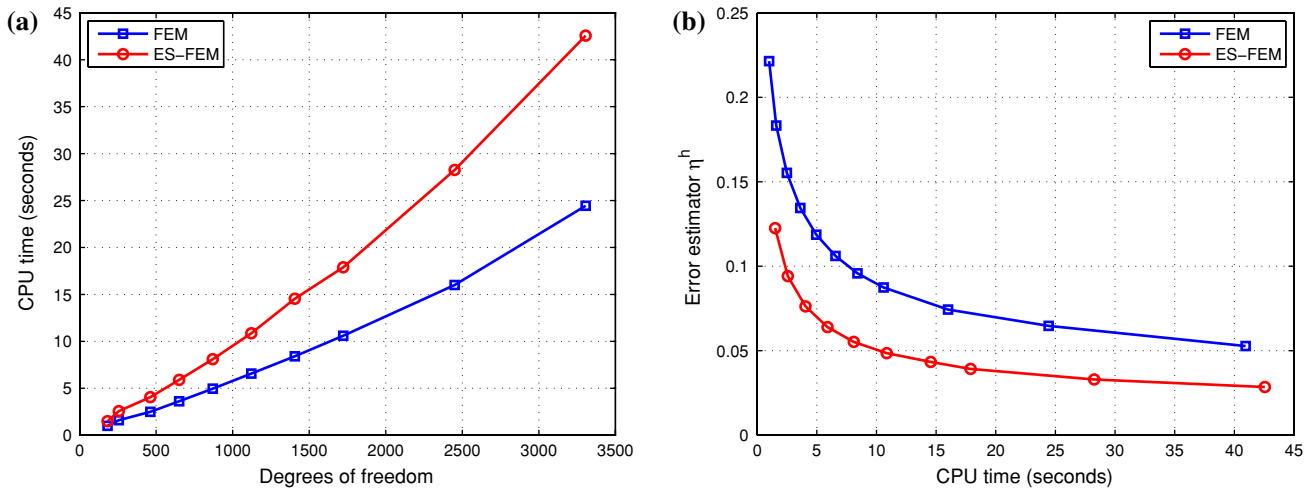

Fig. 9 Comparison of the computational cost and efficiency between the FEM and ES-FEM for a range of meshes at $t = 0.3$ for the plate with hole; **a** Computational cost; **b** Computational efficiency

we will use the following efficient a-posteriori error estimation [2,3]

$$\eta^h = \frac{\left\|\mathbf{R}\boldsymbol{\sigma}^h - \boldsymbol{\sigma}^h\right\|_{L_2(\Omega)}}{\left\|\boldsymbol{\sigma}^h\right\|_{L_2(\Omega)}} = \frac{\left(\sum_{e=1}^{N_e}\int_{\Omega_e}\left(\mathbf{R}\boldsymbol{\sigma}^h - \boldsymbol{\sigma}^h\right):\left(\mathbf{R}\boldsymbol{\sigma}^h - \boldsymbol{\sigma}^h\right)d\Omega\right)^{1/2}}{\left(\sum_{e=1}^{N_e}\int_{\Omega_e}\boldsymbol{\sigma}^h:\boldsymbol{\sigma}^h d\Omega\right)^{1/2}} \quad (56)$$

where $\mathbf{R}\boldsymbol{\sigma}^h$ is a globally continuous recovery stress field derived from the discrete (discontinuous) numerical element stress field $\boldsymbol{\sigma}^h$. The quantity η^h can monitor the local spatial approximation error, and a larger value of η^h implies a larger spatial error.

For the ES-FEM, when computing the stresses $\boldsymbol{\sigma}^h$ for an element, we can average those stresses of smoothing domains of the element, and the averaged stresses are regarded as the stresses of the element as shown in Fig. 6. Similarly, to calculate numerical stresses $\boldsymbol{\sigma}^h(\mathbf{x}_j)$ at a node $\mathbf{x}_j$, we simply average the stresses of smoothing domains associated with the node as shown in Fig. 6. For the FEM, we can regard the stresses at the centroid as the element stresses $\boldsymbol{\sigma}^h$, while the stresses $\boldsymbol{\sigma}^h(\mathbf{x}_j)$ at a node $\mathbf{x}_j$ are the averaged stresses of those of the elements surrounding the node as shown in Fig. 6.

The recovery stress field $\mathbf{R}\boldsymbol{\sigma}^h$ in Eq. (56) for each element in the ES-FEM and the FEM now can be derived from the numerical stresses $\boldsymbol{\sigma}^h\left(\mathbf{x}_j\right)$ at the node $\mathbf{x}_j$ by using the following approximation

$$\mathbf{R}\boldsymbol{\sigma}^h = \sum_{j=1}^{3}\mathbf{N}_j\left(\mathbf{x}\right)\boldsymbol{\sigma}^h\left(\mathbf{x}_j\right) \quad (57)$$

where $\mathbf{N}_j(\mathbf{x})$ are the linear shape functions of triangles used in the standard FEM, and $\boldsymbol{\sigma}^h(\mathbf{x}_j)$ are stress values at three nodes of the element.

In order to evaluate the integrals in Eq. (56) for triangular elements, the mapping procedure using Gauss integration is performed on each element with a summation on all elements. In each element, a proper number of Gauss points depending on the order of the recovery solution $\mathbf{R}\boldsymbol{\sigma}^h$ will be used.

4 Numerical examples

In this section, some numerical examples will be presented to demonstrate the properties of the ES-FEM for visco-elastoplastic analyses. To emphasize the superior properties of the present method, the ES-FEM will be compared to the standard FEM by Carstensen and Klose [2].

4.1 Plate with a circular hole: perfect visco-elastoplasticity

Figure 7 represents a plate $\Omega = [-2, 2] \times [-2, 2]$ with a central circular hole, radius $a = 1\,m$, subjected to time dependent surface forces $g(t) = 500t$ to outer normal at the top and the bottom edges. The rest of the boundary is free. Due to its symmetry, only the upper right quadrant of the plate is modeled. Symmetric conditions are imposed on the left and bottom edges, and the inner boundary of the hole is traction free. Figure 8 gives a discretization of the domain using 561 nodes and 1,024 triangular elements. Assuming that the material is perfect viscoplasticity with Young's modulus $E = 206,900$, Poisson's ratio $v = 0.29$, yield stress $\sigma_Y = 450$ and the initial data for the stress vector $\boldsymbol{\sigma}_0$ is set zero.

The solution is computed in the time interval from $t = 0$ to $t = 0.3$ in 10 uniform steps of time $\Delta t = 0.03$. Using the mesh as shown in Fig. 8, the material remains elastic in six first steps, between $t = 0$ and $t = 0.18$ for both the ES-FEM and FEM as shown in Table 1, because the number of iterations at these times is 1. Table 1 also shows that the number of iterations in Newton's method of both ES-FEM and FEM are almost the same, but the estimated errors η^h in Eq. (56) of the ES-FEM are more than two times less than those of FEM. In addition, Fig. 9 compares the computational cost and efficiency between the FEM and ES-FEM for a range of meshes at $t = 0.3$. It is seen that with the same mesh, the computational cost of ES-FEM is larger than that of FEM as shown in Fig. 9a. However, when the efficiency of computation (computation time for the same accuracy) in terms of the error estimator versus computational cost for a range of meshes is considered, the ES-FEM is more efficient than the FEM as shown in Fig. 9b.

Figure 10 shows the elastic shear energy density $\|\text{dev}(\mathbf{R}\boldsymbol{\sigma}^h)\|^2/(4\mu)$ using the FEM and ES-FEM at $t = 0.3$. The plasticity domain first appears at the corner containing point $A(1, 0)$ and then at the corner containing point $B(0, 1)$. The evolution process of the elastic shear energy density $\|\text{dev}(\mathbf{R}\boldsymbol{\sigma}^h)\|^2/(4\mu)$ can be clearly observed from the ES-FEM results at four different time instances (see Fig. 11). Table 2 compares the displacements of points $A(1, 0)$ and $B(0, 1)$ using FEM and ES-FEM at different time steps. The results show that the displacements of ES-FEM are larger than those of FEM. This implies that the ES-FEM model can reduce the over-stiffness of the standard FEM model using

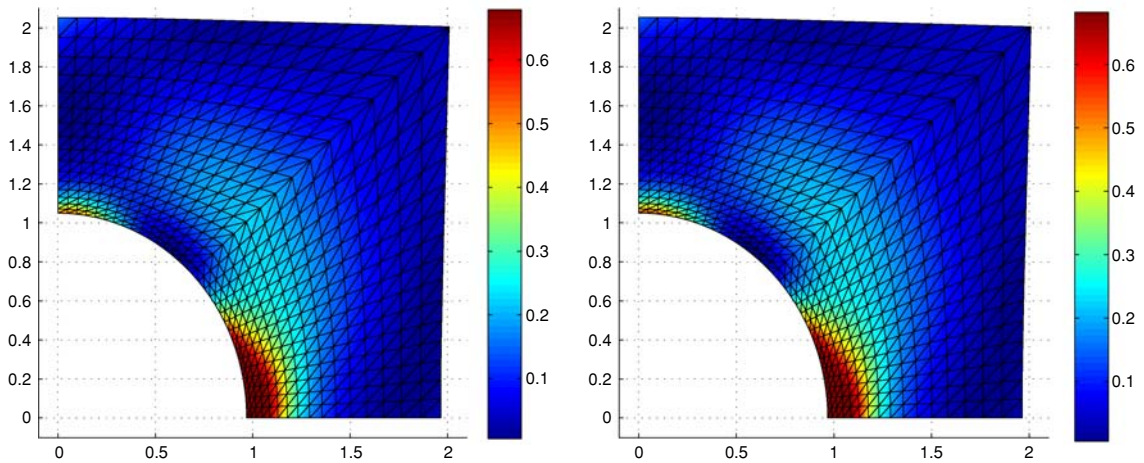

(a) FEM **(b)** ES-FEM

Fig. 10 Elastic shear energy density $\|\text{dev}(\mathbf{R}\boldsymbol{\sigma}^h)\|^2/(4\mu)$ for plate with hole using the FEM (**a**) and ES-FEM (**b**) at $t = 0.3$ (mesh with 561 nodes and 1,024 elements)

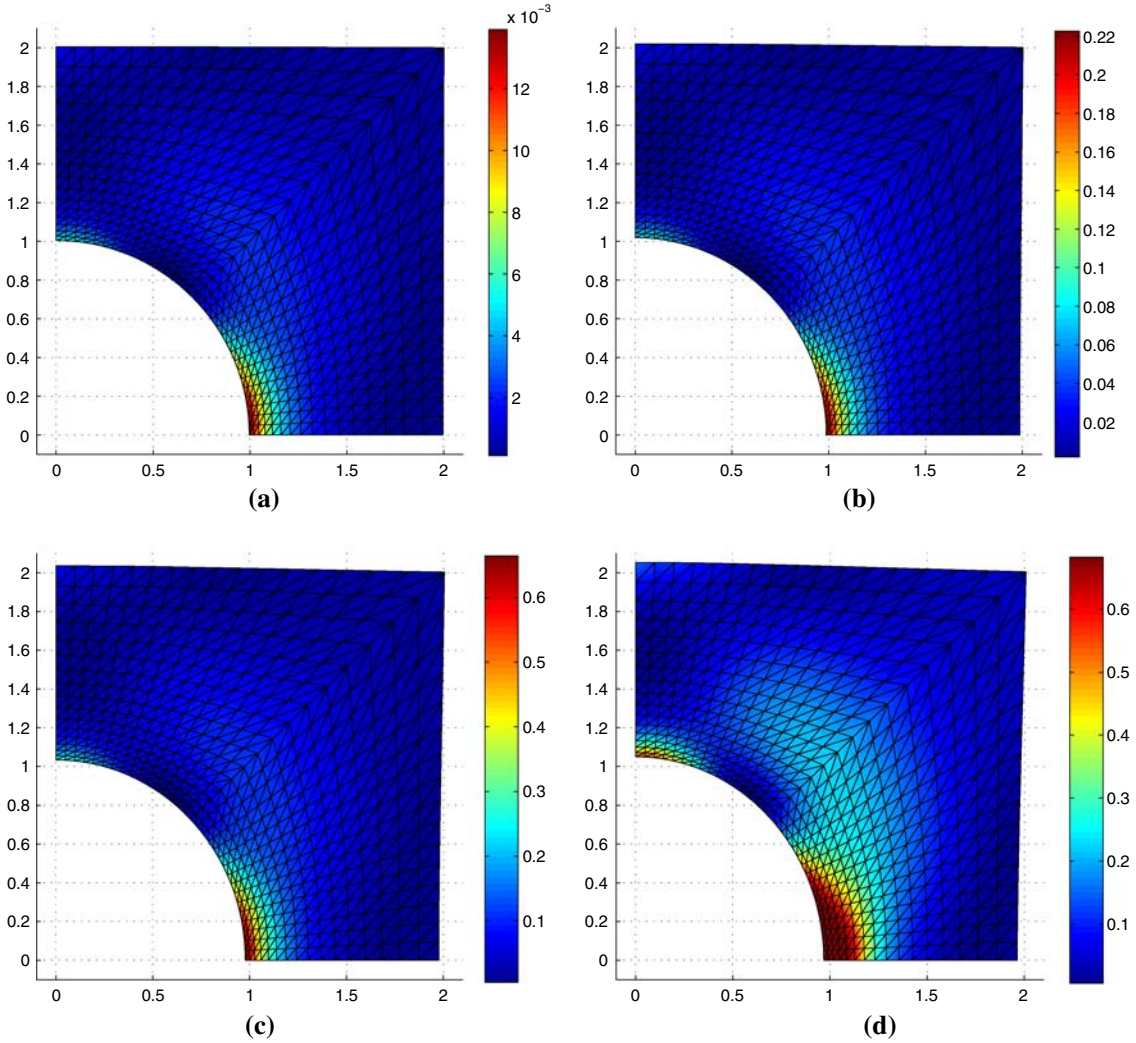

Fig. 11 Elastic shear energy density $\|\mathrm{dev}(\mathbf{R}\boldsymbol{\sigma}^h)\|^2/(4\mu)$ obtained using the ES-FEM at some different time steps for the plate with hole; **a** $t = 0.12$; **b** $t = 0.18$; **c** $t = 0.24$; **d** $t = 0.3$

Table 2 Horizontal displacement u_A at point $A(1, 0)$ and vertical displacement v_B at point $B(0, 1)$ using FEM and ES-FEM at various time steps for the plate with hole

Step	FEM		ES-FEM	
	u_A $(\times 10^{-3})$	v_B $(\times 10^{-3})$	u_A $(\times 10^{-3})$	v_B $(\times 10^{-3})$
1	−0.312	0.4862	−0.316	0.4921
2	−0.624	0.9724	−0.632	0.9842
3	−0.936	1.4586	−0.949	1.4763
4	−1.248	1.9448	−1.265	1.9684
5	−1.560	2.4311	−1.581	2.4605
6	−1.871	2.9173	−1.897	2.9526
7	−2.184	3.4038	−2.214	3.4450
8	−2.503	3.9016	−2.536	3.9530
9	−2.823	4.4286	−2.861	4.4947
10	−3.159	4.9956	−3.183	5.0833

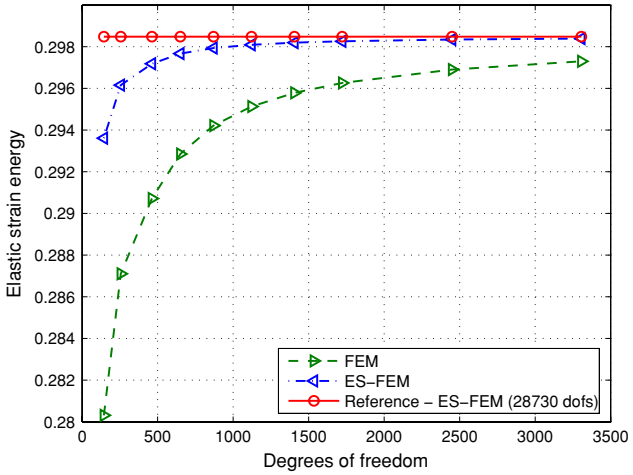

Fig. 12 Convergence of the elastic strain energy $E = \int_\Omega \boldsymbol{\sigma}_\vartheta : \mathbf{e}_\vartheta \, d\Omega$ versus the number of degrees of freedom using the FEM and ES-FEM at $t = 0.3$ for the plate with hole

triangular elements. This property was found earlier for linear elastic problems by Liu et al. [14].

Figure 12 shows the convergence of the elastic strain energy $E = \int_\Omega \boldsymbol{\sigma}_\vartheta : \mathbf{e}_\vartheta \, d\Omega$ versus the number of degrees of freedom using the FEM and ES-FEM at $t = 0.3$. The solution of the ES-FEM using a very fine mesh including 28,730 degrees of freedom is used as reference solution. The results show clearly that the ES-FEM model is much softer and gives more accurate results than the FEM model using triangular elements, especially for the coarse meshes.

4.2 Cook's membrane problem: visco-elastoplasticity with isotropic hardening

This benchmark problem, shown in Fig. 13, refers to a clamped tapered panel subjected to an in-plane shearing load $g(t) = e^{3t}/40$ on the opposite end ($x = 48$) with vanishing volume force f. Figure 13 also gives a discretization of

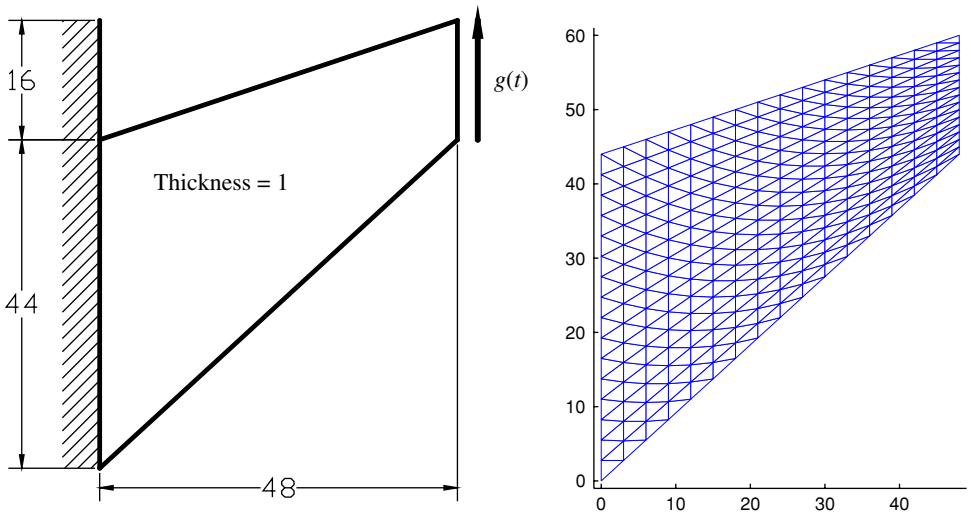

Fig. 13 Cook's membrane problem and its dicretization using 289 nodes and 512 triangular elements

Table 3 Number of iterations and the estimated error using the FEM and ES-FEM at various time steps for Cook's membrane problem

Step	FEM		ES-FEM	
	Iterations	$\eta^h = \frac{\|\mathbf{R}\boldsymbol{\sigma}^h - \boldsymbol{\sigma}^h\|_{L_2(\Omega)}}{\|\boldsymbol{\sigma}^h\|_{L_2(\Omega)}}$	Iterations	$\eta^h = \frac{\|\mathbf{R}\boldsymbol{\sigma}^h - \boldsymbol{\sigma}^h\|_{L_2(\Omega)}}{\|\boldsymbol{\sigma}^h\|_{L_2(\Omega)}}$
1	1	0.197645	1	0.076465
2	1	0.197645	1	0.076465
3	3	0.197646	3	0.076469
4	3	0.197650	3	0.076469
5	3	0.197652	3	0.076466
6	3	0.197654	3	0.076453
7	3	0.197656	3	0.076431
8	4	0.197660	4	0.076402
9	4	0.197671	4	0.076366
10	4	0.197690	4	0.076325

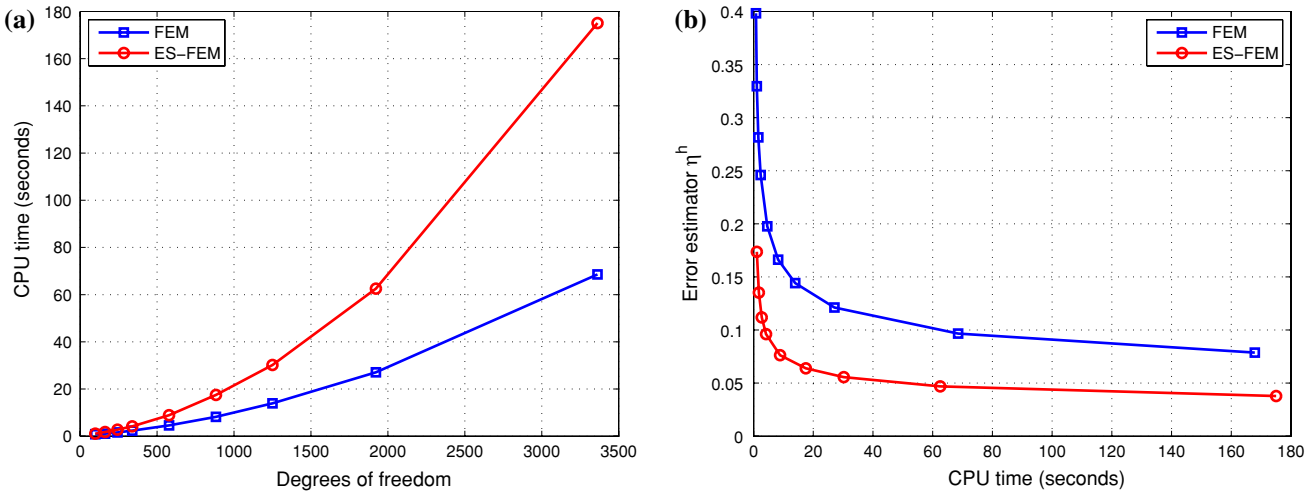

Fig. 14 Comparison of the computational cost and efficiency between the FEM and ES-FEM for a range of meshes at $t = 0.25$ for the Cook's membrane problem; **a** Computational cost; **b** Computational efficiency

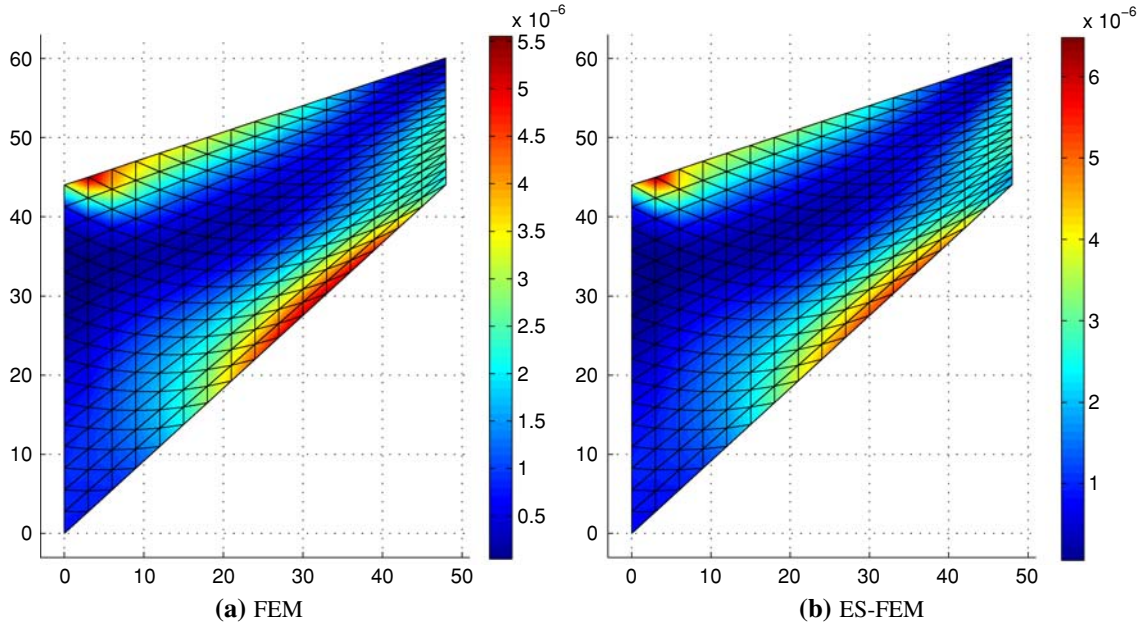

Fig. 15 Elastic shear energy density $\|\mathrm{dev}(\mathbf{R}\boldsymbol{\sigma}^h)\|^2/(4\mu)$ for Cook's membrane problem using the FEM (**a**) and ES-FEM (**b**) at $t = 0.25$ (mesh with 289 nodes, 512 elements)

the domain using 289 nodes and 512 triangular elements. Assuming that the material is isotropic hardening viscoplasticity with Young's modulus $E = 2{,}900$, Poisson's ratio $\upsilon = 0.4$, yield stress $\sigma_Y = 0.1$, $H = 1{,}000$, $H_1 = 1$; and the initial data for the stress vector $\boldsymbol{\sigma}_0$ and the scalar hardening parameter α_0^I are set zero.

The solution is calculated in the time interval from $t = 0$ to $t = 0.25$ in 10 uniform steps of time $\Delta t = 0.025$. Using the mesh as shown in Fig. 13, the material remains elastic in two first steps, between $t = 0$ and $t = 0.05$ for both ES-FEM and FEM as shown in Table 3. Table 3 also shows that the number of iterations in Newton's method of both ES-FEM and FEM are almost the same, but the estimated errors η^h in Eq. (56) of ES-FEM are about three times less than those of FEM. In addition, Fig. 14 compares the computational cost and efficiency between the FEM and ES-FEM for a range of meshes at $t = 0.25$. It is seen that with the same mesh, the computational cost of ES-FEM is larger than that of FEM as shown in Fig. 14a. However, when the efficiency of computation (computation time for the same accuracy) in terms of

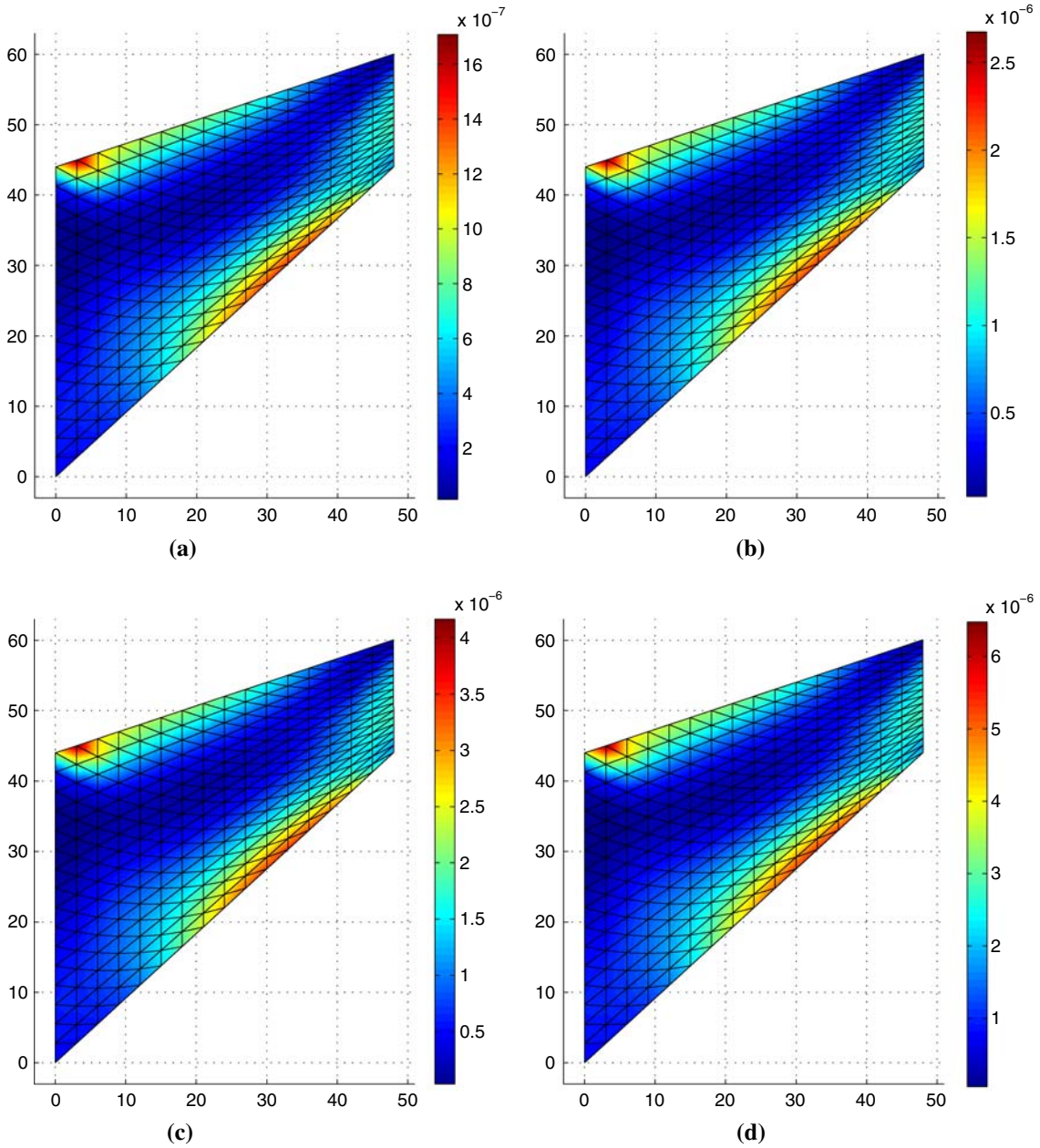

Fig. 16 Elastic shear energy density $\|\mathrm{dev}(\mathbf{R}\boldsymbol{\sigma}^h)\|^2/(4\mu)$ using the ES-FEM at some different time steps for Cook's membrane problem; **a** $t = 0.025$; **b** $t = 0.10$; **c** $t = 0.175$; **d** $t = 0.25$

the error estimator versus computational cost for a range of meshes is considered, the ES-FEM is more efficient than the FEM as shown in Fig. 14b.

Figure 15 shows the elastic shear energy density $\|\mathrm{dev}(\mathbf{R}\boldsymbol{\sigma}^h)\|^2/(4\mu)$ using FEM and ES-FEM at $t = 0.25$ for the mesh as shown in Fig. 13. The evolution process of the elastic shear energy density $\|\mathrm{dev}(\mathbf{R}\boldsymbol{\sigma}^h)\|^2/(4\mu)$ can be clearly observed from the ES-FEM results at four different time instances (see Fig. 16). Table 4 also compares the displacement of point $A(48, 60)$ using the FEM and ES-FEM at different time steps. The results show that the displacements of ES-FEM are larger than those of FEM. This again verifies that the ES-FEM model can reduce the over-stiffness of the standard FEM model using triangular elements.

Figure 17 shows the convergence of the elastic strain energy $E = \int_\Omega \boldsymbol{\sigma}_\vartheta : \mathbf{e}_\vartheta d\Omega$ versus the number of degrees of freedom using the FEM and ES-FEM at $t = 0.25$. The solution of ES-FEM using a very fine mesh including 26,041 degrees of freedom is used as reference solution. The results again show clearly that the ES-FEM model is much softer and gives more accurate results than the FEM model using triangular elements, especially for the coarse meshes.

Table 4 Displacement at point $A(48, 60)$ using the FEM and ES-FEM at various time steps for Cook's membrane problem

Step	FEM		ES-FEM	
	u_A	v_A	u_A	v_A
1	−0.0022	0.0031	−0.0023	0.0032
2	−0.0024	0.0033	−0.0025	0.0034
3	−0.0026	0.0035	−0.0027	0.0037
4	−0.0028	0.0038	−0.0029	0.0040
5	−0.0030	0.0041	−0.0031	0.0043
6	−0.0032	0.0044	−0.0034	0.0046
7	−0.0035	0.0048	−0.0036	0.0049
8	−0.0037	0.0052	−0.0039	0.0053
9	−0.0040	0.0056	−0.0042	0.0057
10	−0.0043	0.0060	−0.0045	0.0062

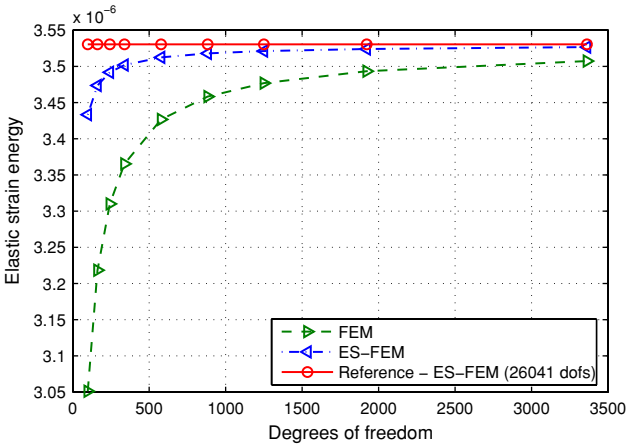

Fig. 17 Convergence of the elastic strain energy $E = \int_\Omega \boldsymbol{\sigma}_\vartheta : \mathbf{e}_\vartheta d\Omega$ versus the number of degrees of freedom using the FEM and ES-FEM at $t = 0.25$ for Cook's membrane problem

4.3 Axis-symmetric ring: visco-elastoplasticity with linear kinematic hardening

Figure 18 shows a thick axis-symmetric ring, with internal radius $a = 1$, external radius $b = 2$, subjected to time depending surface forces $g_1(r, \varphi, t) = te_r$ on inner radius and $g_2(r, \varphi, t) = -te_r/4$ on outer radius with $e_r = (\cos\varphi, \sin\varphi)$. There is no body force. For this problem, the exact solution [2] is

$$\begin{aligned} u(r, \varphi, t) &= u_r(r, t)\, e_r \\ \sigma(r, \varphi, t) &= \sigma_r(r, t)\, e_r \otimes e_r + \sigma_\varphi e_\varphi \otimes e_\varphi \\ p(r, \varphi, t) &= P_r(r, t)\left(e_r \otimes e_r - e_\varphi \otimes e_\varphi\right) \end{aligned} \tag{58}$$

where $e_r = (\cos\varphi, \sin\varphi)$, $e_\varphi = (-\sin\varphi, \cos\varphi)$ and

$$u_r(r, t) = \begin{cases} \dfrac{t}{2\mu r} - \dfrac{1}{3}\psi I(R(t))\left(r + \dfrac{4a}{\mu r}\right) & \text{for } r \geq R(t) \\ \dfrac{t}{2\mu r} - \dfrac{1}{3}\psi I(R(t)) & \\ \quad \left(4r + \dfrac{4a}{\mu r}\right) + \psi I(r)\, r & \text{for } r < R(t) \end{cases} \tag{59}$$

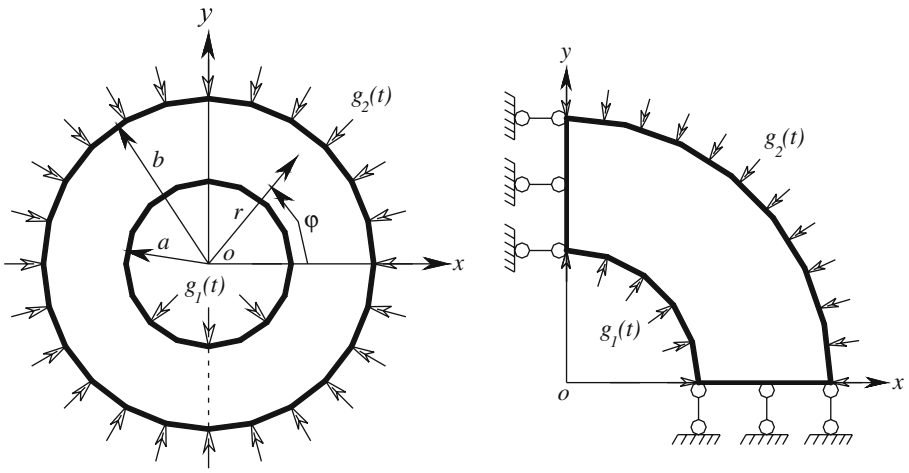

Fig. 18 The axis-symmetric ring subjected to time dependent surface forces $g_1(t)$ on inner radius and $g_2(t)$ on outer radius and its quarter model with symmetric conditions imposed on the left and bottom edges

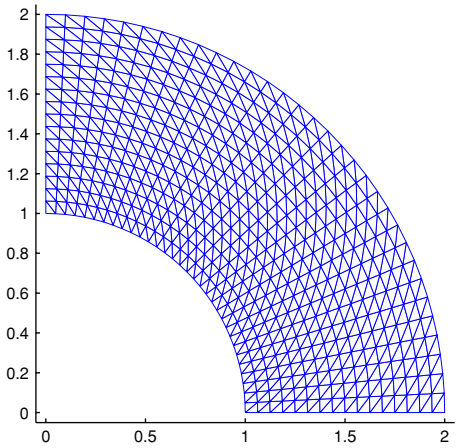

Fig. 19 Domain discretization of one quarter of the axis-symmetric ring using 561 nodes and 1,024 triangular elements

$$\sigma_r(r,t) = \begin{cases} -\dfrac{t}{r^2} - \dfrac{8}{3}a\psi I(R(t))\left(\dfrac{1}{4} - \dfrac{1}{r^2}\right) & \text{for } r \geq R(t) \\ -\dfrac{t}{r^2} - \dfrac{8}{3}a\psi I(R(t))\left(1 - \dfrac{1}{r^2}\right) & \\ \quad +2a\psi I(r) & \text{for } r < R(t) \end{cases} \tag{60}$$

$$\sigma_\varphi(r,t) = \frac{\partial(r\sigma_r)}{\partial r} \tag{61}$$

$$P_r(r,t) = \begin{cases} 0 & \text{for } r \geq R(t) \\ \dfrac{\sigma_y}{\sqrt{2}(a\psi + k_1)}\left(1 - \dfrac{R^2}{r^2}\right) & \text{for } r < R(t) \end{cases} \tag{62}$$

$$I(r) = \frac{\sigma_y}{\sqrt{2}(a\psi + k_1)}\left(\ln r + \frac{1}{2}\left(\frac{R^2}{r^2} - R^2\right)\right) \tag{63}$$

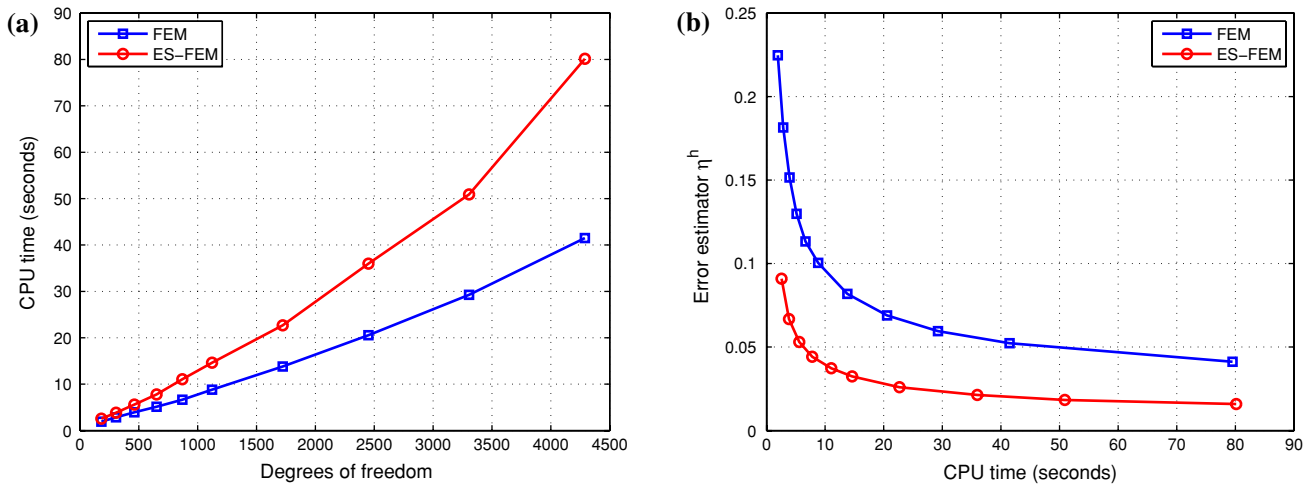

Fig. 20 Comparison of the computational cost and efficiency between the FEM and ES-FEM for a range of meshes at $t = 0.22$ for the axis-symmetric ring problem; **a** Computational cost; **b** Computational efficiency

Table 5 Number of iterations and the estimated error using the FEM and ES-FEM at various time steps for the axis-symmetric ring problem

Step	FEM-T3				ES-FEM			
	Iters	$e = \frac{\|\boldsymbol{\sigma}-\boldsymbol{\sigma}^h\|_{L_2}}{\|\boldsymbol{\sigma}^h\|_{L_2}}$	$\eta^h = \frac{\|\mathbf{R}\boldsymbol{\sigma}^h-\boldsymbol{\sigma}^h\|_{L_2}}{\|\boldsymbol{\sigma}^h\|_{L_2}}$	$\frac{e}{\eta^h}$	Iters	$e = \frac{\|\boldsymbol{\sigma}-\boldsymbol{\sigma}^h\|_{L_2}}{\|\boldsymbol{\sigma}^h\|_{L_2}}$	$\eta^h = \frac{\|\mathbf{R}\boldsymbol{\sigma}^h-\boldsymbol{\sigma}^h\|_{L_2}}{\|\boldsymbol{\sigma}^h\|_{L_2}}$	$\frac{e}{\eta^h}$
1	1	0.079725	0.0792	1.01	1	0.03342	0.0328	1.02
2	1	0.079725	0.0792	1.01	1	0.03342	0.0328	1.02
3	1	0.079725	0.0792	1.01	1	0.03342	0.0328	1.02
4	1	0.079725	0.0792	1.01	1	0.03342	0.0328	1.02
5	1	0.079725	0.0792	1.01	1	0.03342	0.0328	1.02
6	1	0.079725	0.0792	1.01	1	0.03342	0.0328	1.02
7	1	0.079725	0.0792	1.01	1	0.03342	0.0328	1.02
8	3	0.083988	0.0816	1.03	4	0.03376	0.0331	1.02
9	4	0.089265	0.0874	1.02	4	0.03372	0.0340	0.99
10	5	0.095374	0.0933	1.02	4	0.03269	0.0330	0.99
11	5	0.102883	0.1004	1.02	5	0.03206	0.0324	0.99

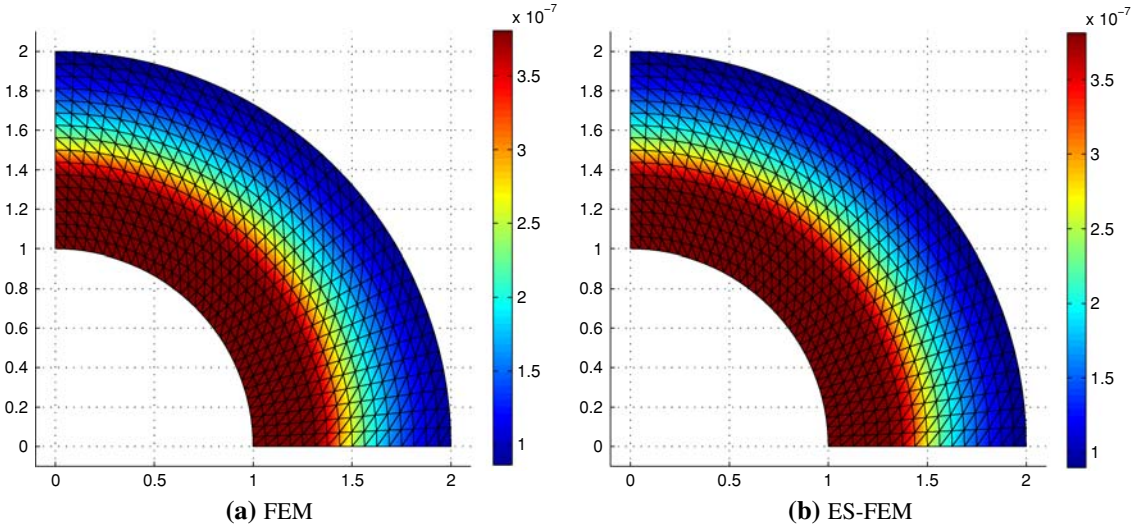

Fig. 21 Elastic shear energy density $\|\mathrm{dev}(\mathbf{R}\boldsymbol{\sigma}^h)\|^2/(4\mu)$ for the axis-symmetric ring problem using the FEM (**a**) and ES-FEM (**b**) at $t = 0.22$ (mesh with 561 nodes and 1,024 triangular elements)

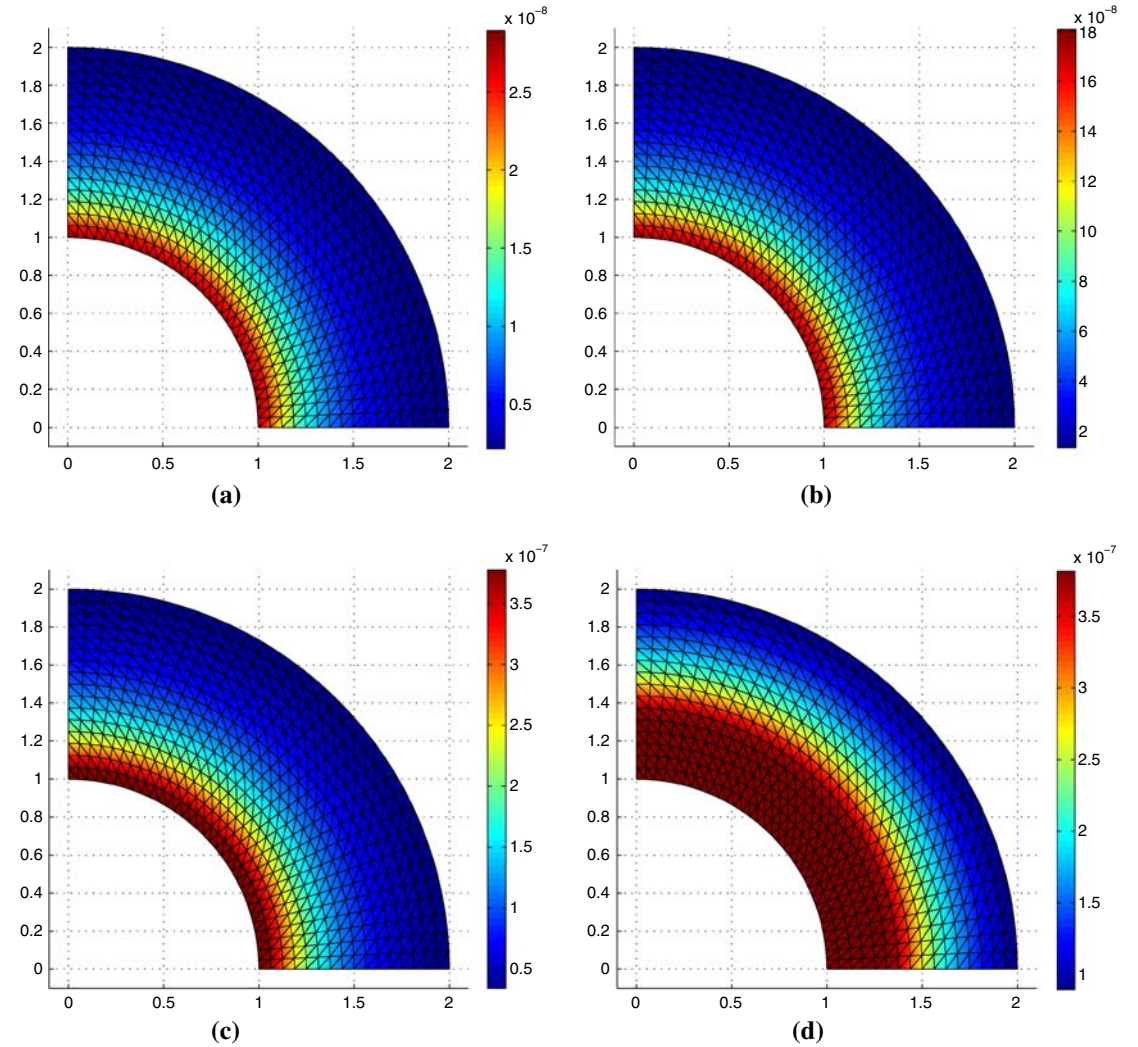

Fig. 22 Evolution of the elastic shear energy density $\|\mathrm{dev}(\mathbf{R}\boldsymbol{\sigma}^h)\|^2/(4\mu)$ using the ES-FEM at some different time steps for the axis-symmetric ring problem; **a** $t = 0.04$; **b** $t = 0.1$; **c** $t = 0.16$; **d** $t = 0.22$

Table 6 Horizontal displacement at point $A(1, 0)$ and vertical displacement at point $B(0, 1)$ using FEM and ES-FEM at various time steps for the axis-symmetric ring problem

Time	FEM				ES-FEM			
	Iterations	u_A	v_B	u_A/v_B	Iterations	u_A	v_B	u_A/v_B
1	1	0.0376	0.0381	0.9866	1	0.0379	0.0380	0.9979
2	1	0.0752	0.0763	0.9866	1	0.0759	0.0760	0.9979
3	1	0.1129	0.1144	0.9866	1	0.1138	0.1141	0.9979
4	1	0.1505	0.1525	0.9866	1	0.1518	0.1521	0.9979
5	1	0.1881	0.1907	0.9866	1	0.1897	0.1901	0.9979
6	1	0.2257	0.2288	0.9866	1	0.2276	0.2281	0.9979
7	1	0.2634	0.2669	0.9866	1	0.2656	0.2662	0.9979
8	3	0.3049	0.3097	0.9845	3	0.3077	0.3091	0.9955
9	4	0.3586	0.3653	0.9817	4	0.3620	0.3642	0.9941
10	5	0.4305	0.4385	0.9819	4	0.4356	0.4386	0.9931
11	5	0.5336	0.5386	0.9906	4	0.5382	0.5422	0.9927

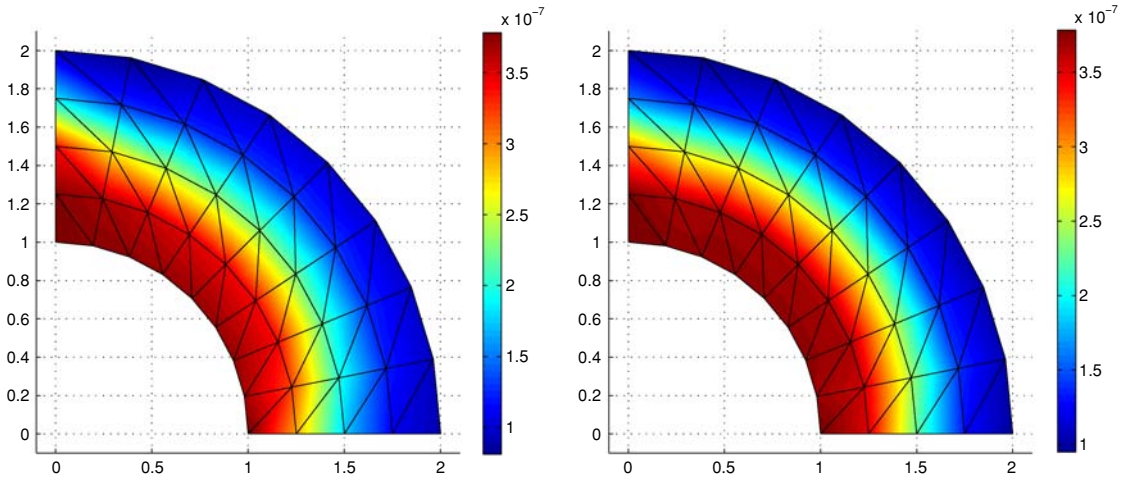

(a) FEM **(b)** ES-FEM

Fig. 23 Elastic shear energy density $\|\text{dev}(\mathbf{R}\boldsymbol{\sigma}^h)\|^2/(4\mu)$ for the axis-symmetric ring problem using the FEM (**a**) and ES-FEM (**b**) at $t = 0.22$ (mesh with 45 nodes and 64 triangular elements)

and $a = \mu + \lambda, \psi = 2\mu/(2\mu + \lambda)$. With $\alpha = 4a\psi/(3(a\psi + k_1))$, the radius of the plastic boundary $R(t)$ is the positive root of

$$f(R) = -2\alpha \ln R + (\alpha - 1)R^2 - \alpha + \frac{\sqrt{2}}{\sigma_y}t \tag{64}$$

Because of the axis-symmetric characteristic of the problem, we only calculate for one quarter of ring as shown in Fig. 18, and symmetric conditions are imposed on the left and bottom edges. Figure 19 gives a discretization of the domain using 561 nodes and 1,024 triangular elements. The material parameters are given with Young's modulus $E = 70{,}000$, Poisson's ratio $\upsilon = 0.33$, yield stress $\sigma_Y = 0.2$, the hardening parameter is $k_1 = 1$, and the initial data for the displacement $\boldsymbol{u}_0$, the stress vector $\boldsymbol{\sigma}_0$ and the hardening parameter $\boldsymbol{\alpha}_0^K$ are set zero.

The solution is calculated in the time interval from $t = 0$ to $t = 0.22$ in 11 uniform steps of time $\Delta t = 0.02$. Using the mesh as shown in Fig. 19, the material remains elastic in seven first steps, between $t = 0$ and $t = 0.14$ for both ES-FEM and FEM as shown in Table 5. The material becomes plastic at $t = 0.16$. Table 5 also shows the exact error e and estimated error η^h for the different time steps together with the number of iterations in Newton's method. The results show that the ratio e/η^h almost equals 1 for all iterations which implies that the estimated error η^h can be regarded as an accurate error estimator. This example therefore asserts the reliability of the estimated error η^h used in this work.

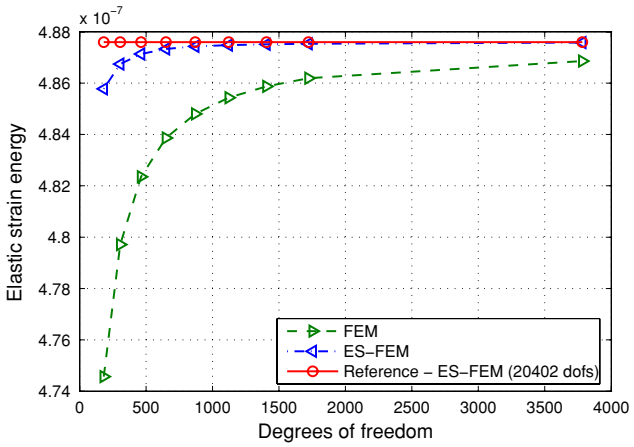

Fig. 24 Convergence of the elastic strain energy $E = \int_\Omega \boldsymbol{\sigma}_\vartheta : \mathbf{e}_\vartheta d\Omega$ versus the number of degrees of freedom using the FEM and ES-FEM at $t = 0.22$ for the axis-symmetric ring problem

In addition, the results also shows that the number of iterations in Newton's method of both ES-FEM and FEM are almost the same, but the estimated errors η^h in Eq. (56) of the ES-FEM are about three times less than those of FEM. Furthermore, Fig. 20 compares the computational cost and efficiency between the FEM and ES-FEM for a range of meshes at $t = 0.22$. It is seen that with the same mesh, the computational cost of ES-FEM is larger than that of FEM as shown in Fig. 20a. However, when the efficiency of computation (computation time for the same accuracy) in terms of the error estimator versus computational cost for a range of meshes is considered, the ES-FEM is more efficient than the FEM as shown in Fig. 20b.

Figure 21 shows the elastic shear energy density $\|\text{dev}(\mathbf{R}\boldsymbol{\sigma}^h)\|^2/(4\mu)$ using FEM and ES-FEM at $t = 0.22$. The plastic domain first appears at the inner radius and extents toward the outer radius. The evolution process of the elastic shear energy density $\|\text{dev}(\mathbf{R}\boldsymbol{\sigma}^h)\|^2/(4\mu)$ can be clearly observed from the ES-FEM results at four different time instances (see Fig. 22). Table 6 shows the ratio of radial displacements between points $A(1, 0)$ and $B(0, 1)$ using the FEM and ES-FEM at various time steps. It is seen that for the symmetric problem, the results of ES-FEM is more symmetric than those of FEM. This finding is also supported by the solution of the elastic shear energy density $\|\text{dev}(\mathbf{R}\boldsymbol{\sigma}^h)\|^2/(4\mu)$ shown as contour in Fig. 23 obtained using a coarse mesh with 45 nodes and 64 triangular elements.

Figure 24 shows the convergence of the elastic strain energy $E = \int_\Omega \boldsymbol{\sigma}_\vartheta : \mathbf{e}_\vartheta d\Omega$ versus the number of degrees of freedom using the FEM and ES-FEM at $t = 0.22$. The results again verify that the ES-FEM model is much softer and gives more accurate results than the FEM model using triangular elements, especially for the coarse meshes.

5 Conclusion

In this paper, the ES-FEM is extended to more complicated visco-elastoplastic analyses. We combine the ES-FEM using triangular elements with the work of Carstensen and Klose [2] in the setting of von-Mises conditions and the Prandtl–Reuss flow rule, and the material behavior includes perfect visco-elastoplasticity, and visco-elastoplasticity with isotropic and linear kinematic hardening in a dual model, with displacements and the stresses as the main variables. The numerical procedure, however, eliminates the stress variables and the problem becomes only displacement-dependent and is much easy to deal with. The numerical results of ES-FEM using triangular elements show that

- The displacement results of ES-FEM are larger than those of FEM. The elastic strain energy of ES-FEM is much more accurate than that of FEM. These results show clearly that the ES-FEM model can reduce the over-stiffness of the standard FEM model using triangular elements and gives much more accurate results than those of FEM. These properties were demonstrated for the static, free and forced vibration analyses of elastic solids by Liu et al. [14].
- The a-posteriori estimated error η^h used in this work is shown to be reliable to represent the accurate error estimator. The bandwidth of stiffness matrix of ES-FEM is larger than that of FEM, and hence the computational cost of ES-FEM is larger than that of FEM. However, when the efficiency of computation (computation time for the same accuracy) in terms of the a-posteriori error estimation is considered, the ES-FEM is more efficient than the FEM.
- For the coarse meshes, the results of ES-FEM are much more accurate than those of FEM.
- For the axis-symmetric problems, the results of ES-FEM are more symmetric than those of FEM.

Acknowledgments This work is partially supported by A*Star, Singapore. It is also partially supported by the Open Research Fund Program of the State Key Laboratory of Advanced Technology of Design and Manufacturing for Vehicle Body, Hunan University, P.R.China under the grant number 40915001.

References

1. Bordas S, Rabczuk T, Nguyen-Xuan H, Nguyen Vinh P, Natarajan S, Bog T, Do Minh Q, Nguyen Vinh H (2009) Strain smoothing in FEM and XFEM. Comput Struct. doi:10.1016/j.compstruc.2008.07.006
2. Carstensen C, Klose R (2002) Elastoviscoplastic finite element analysis in 100 lines of matlab. J Numer Math 10:157–192

3. Carstensen C, Funken SA (2001) Averaging technique for FE-a posteriori error control in elasticity. Part 1: conforming FEM. Comput Methods Appl Mech Eng 190:2483–2498
4. Chen JS, Wu CT, Yoon S, You Y (2001) A stabilized conforming nodal integration for Galerkin meshfree method. Int J Numer Methods Eng 50:435–466
5. Cui XY, Liu GR, Li GY, Zhao X, Nguyen-Thoi T, Sun GY (2008) A smoothed finite element method (SFEM) for linear and geometrically nonlinear analysis of plates and shells. CMES-Comput Model Eng Sci 28(2):109–125
6. Dai KY, Liu GR (2007) Free and forced analysis using the smoothed finite element method (SFEM). J Sound Vib 301:803–820
7. Dai KY, Liu GR, Nguyen-Thoi T (2007) An *n*-sided polygonal smoothed finite element method (nSFEM) for solid mechanics. Finite Elements Anal Des 43:847–860
8. Dohrmann CR, Heinstein MW, Jung J, Key SW, Witkowski WR (2000) Node-based uniform strain elements for three-node triangular and four-node tetrahedral meshes. Int J Numer Methods Eng 47:1549–1568
9. Liu GR (2008) A generalized gradient smoothing technique and the smoothed bilinear form for Galerkin formulation of a wide class of computational methods. Int J Comput Methods 5(2):199–236
10. Liu GR, Dai KY, Nguyen-Thoi T (2007) A smoothed finite element method for mechanics problems. Comput Mech 39:859–877
11. Liu GR, Li Y, Dai KY, Luan MT, Xue W (2006) A Linearly conforming radial point interpolation method for solid mechanics problems. Int J Comput Methods 3(4):401–428
12. Liu GR, Nguyen-Thoi T, Dai KY, Lam KY (2007) Theoretical aspects of the smoothed finite element method (SFEM). Int J Numer Methods Eng 71:902–930
13. Liu GR, Nguyen-Thoi T, Lam KY (2008) A novel alpha finite element method (αFEM) for exact solution to mechanics problems using triangular and tetrahedral elements. Comput Methods Appl Mech Eng 197:3883–3897
14. Liu GR, Nguyen-Thoi T, Lam KY (2009) An edge-based smoothed finite element method (ES-FEM) for static, free and forced vibration analyses of solids. J Sound Vib 320:1100–1130
15. Liu GR, Nguyen-Thoi T, Nguyen-Xuan H, Lam KY (2009) A node-based smoothed finite element method for upper bound solution to solid problems (NS-FEM). Comput Struct 87:14–26
16. Liu GR, Zhang GY (2008) Upper bound solution to elasticity problems: a unique property of the linearly conforming point interpolation method (LC-PIM). Int J Numer Methods Eng 74:1128–1161
17. Liu GR, Zhang GY, Dai KY, Wang YY, Zhong ZH, Li GY, Han X (2005) A linearly conforming point interpolation method (LC-PIM) for 2D solid mechanics problems. Int J Comput Methods 2(4):645–665
18. Liu GR, Zhang GY, Wang YY, Huang HT, Zhong ZH, Li GY, Han X (2007) A linearly conforming point interpolation method (LC-PIM) for three-dimensional elasticity problems. Int J Numer Methods Eng 72:1524–1543
19. Nguyen-Thanh N, Rabczuk T, Nguyen-Xuan H, Bordas S (2008) A smoothed finite element method for shell analysis. Comput Methods Appl Mech Eng 198:165–177
20. Nguyen-Thoi T, Liu GR, Dai KY, Lam KY (2007) Selective smoothed finite element method. Tsinghua Sci Technol 12(5):497–508
21. Nguyen-Thoi T, Liu GR, Lam KY, Zhang GY (2009) A face-based smoothed finite element method (FS-FEM) for 3D linear and nonlinear solid mechanics problems using 4-node tetrahedral elements. Int J Numer Methods Eng 78:324–353
22. Nguyen-Thoi T, Liu GR, Nguyen-Xuan H, Nguyen-Tran C (2009) Adaptive analysis using the node-based smoothed finite element method (NS-FEM). Commun Numer Methods Eng. doi:10.1002/cnm.1291
23. Nguyen-Thoi T, Liu GR, Vu-Do HC, Nguyen-Xuan H (2009) A face-based smoothed finite element method (FS-FEM) for 3D visco-elastoplastic analyses of solid using tetrahedral mesh. Comput Methods Appl Mech Eng. doi:10.1016/j.cma.2009.07.001
24. Nguyen-Van H, Mai-Duy N, Tran-Cong T (2008) A smoothed four-node piezoelectric element for analysis of two-dimensional smart structures. CMES-Comput Model Eng Sci 23(3):209–222
25. Nguyen-Xuan H, Bordas S, Nguyen-Dang H (2008) Addressing volumetric locking and instabilities by selective integration in smoothed finite elements. Commun Numer Methods Eng 25:19–34
26. Nguyen-Xuan H, GR Liu, Nguyen-Thoi T, Nguyen-Tran C (2009) An edge–based smoothed finite element method (ES-FEM) for analysis of two–dimensional piezoelectric structures. Smart Mater Struct 18:065015 (12pp)
27. Nguyen-Xuan H, Liu GR, Thai-Hoang C, Nguyen-Thoi T (2009) An edge-based smoothed finite element method with stabilized discrete shear gap technique for analysis of Reissner–Mindlin plates. Comput Methods Appl Mech Eng (revised)
28. Nguyen-Xuan H, Rabczuk T, Bordas S, Debongnie JF (2008) A smoothed finite element method for plate analysis. Comput Methods Appl Mech Eng 197:1184–1203
29. Nguyen-Xuan H, Nguyen-Thoi T (2009) A stabilized smoothed finite element method for free vibration analysis of Mindlin–Reissner plates. Commun Numer Methods Eng 25:882–906
30. Tran Thanh Ngoc, Liu GR, Nguyen-Xuan H, Nguyen-Thoi T (2009) An edge-based smoothed finite element method for primal-dual shakedown analysis of structures. Int J Numer Methods Eng (revised)
31. Yoo JW, Moran B, Chen JS (2004) Stabilized conforming nodal integration in the natural-element method. Int J Numer Methods Eng 60:861–890